J. Fluid Mech. (2005), *vol.* 523, *pp.* 277–306. © 2005 Cambridge University Press
DOI: 10.1017/S0022112004002150 Printed in the United Kingdom

Instability-induced ordering, universal unfolding and the role of gravity in granular Couette flow

By MEHEBOOB ALAM[1]†, V. H. ARAKERI[2], P. R. NOTT[3], J. D. GODDARD[4] AND H. J. HERRMANN[5]

[1]Engineering Mechanics Unit, Jawaharlal Nehru Center for Advanced Scientific Research Jakkur P.O., Bangalore 560064, India

[2]Department of Mechanical Engineering, IISc, Bangalore 560012, India

[3]Department of Chemical Engineering, IISc, Bangalore 560012, India

[4]Department of Mechanical Engineering, UCSD, La Jolla, CA 92093

[5]ICA1, Universität Stuttgart, Pfaffenwaldring 27, D 70569 Stuttgart, Germany

(Received 4 February 2004 and in revised form 23 August 2004)

Linear stability theory and bifurcation analysis are used to investigate the role of gravity in shear-band formation in granular Couette flow, considering a kinetic-theory rheological model. We show that the only possible state, at low shear rates, corresponds to a 'plug' near the bottom wall, in which the particles are densely packed and the shear rate is close to zero, and a uniformly sheared dilute region above it. The origin of such plugged states is shown to be tied to the spontaneous symmetry-breaking instabilities of the gravity-free uniform shear flow, leading to the formation of ordered bands of alternating dilute and dense regions in the transverse direction, via an infinite hierarchy of pitchfork bifurcations. Gravity plays the role of an 'imperfection', thus destroying the 'perfect' bifurcation structure of uniform shear. The present bifurcation problem admits universal unfolding of pitchfork bifurcations which subsequently leads to the formation of a sequence of a countably infinite number of 'isolas', with the solution structures being a modulated version of their gravity-free counterpart. While the solution with a plug near the bottom wall looks remarkably similar to the shear-banding phenomenon in dense slow granular Couette flows, a 'floating' plug near the top wall is also a solution of these equations at high shear rates. A two-dimensional linear stability analysis suggests that these floating plugged states are unstable to long-wave travelling disturbances.The unique solution having a bottom plug can also be unstable to long waves, but remains stable at sufficiently low shear rates. The implications and realizability of the present results are discussed in the light of shear-cell experiments under 'microgravity' conditions.

1. Introduction

Instability-induced pattern formation has been extensively studied in classical fluid mechanics. For rapid granular flows, which may aptly be described by the dissipative analogue of compressible fluid equations (see, for reviews, Campbell 1990; Hutter & Rajagopal 1994; Jaeger, Nagel & Behringer 1996; Herrmann, Hovi & Luding 1998; Kadanoff 1999; Pöschel & Luding 2001), such studies are relatively

† Author to whom all correspondence should be addressed: meheboob@jncasr.ac.in

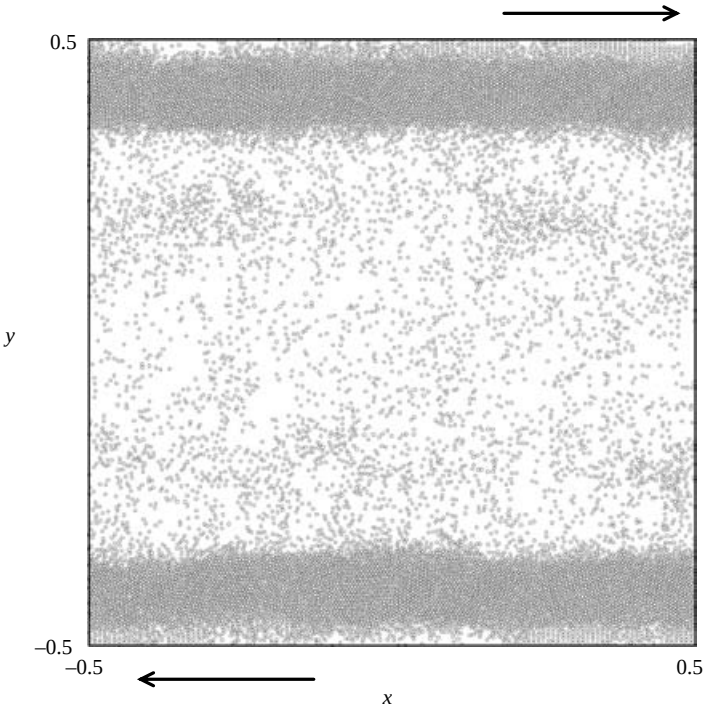

FIGURE 1. Formation of ordered plugs in event-driven simulations of a sheared inelastic hard-disk system. The average solid fraction is $\overline{\nu} = 0.3$, the restitution coefficient $e = 0.8$ and the total number of particles 15000.

new (Savage 1992; Babic 1993; Schmid & Kytömaa 1994; Alam & Nott 1997, 1998; Nott *et al.* 1999; Forterre & Pouliquen 2002; Alam 2003). For experiments on flows down an inclined plane, many interesting patterns in the form of roll waves, Kelvin–Helmholtz instability, fingering instability and streamwise vortices (Forterre & Pouliquen 2002; Goldfarb, Glasser & Shinbrot 2002) have recently been reported. Observations of cluster formation, density-waves and stress-fluctuations in computer simulations of granular shear flows (Hopkins & Louge 1991; Peng & Herrmann 1996; Luding & Herrmann 1999) have stimulated subsequent theoretical works on the associated macroscopic flows described by suitable continuum equations (Savage 1992; Alam & Nott 1997, 1998; Nott *et al.* 1999); to this end, the kinetic-theory-based rheological models (Lun *et al.* 1984; Jenkins & Richman 1986; Sela & Goldhirsch 1998; Hayakawa 2003) have routinely been used. One major goal of these theoretical works has been to see whether a hydrodynamic description holds for a gramular fluid, via testing the available rheological models from the viewpoint of pattern formation.

To motivate the present work, we show a typical snapshot of a sheared system of inelastic smooth hard disks (in a gravity-free environment) in figure 1. Event-driven simulations (Alam 2003; Alam & Luding 2003) were used: the mean volume fraction of particles is $\overline{\nu} = 0.3$, the coefficient of restitution $e = 0.8$ and the total number of particles 15 000. From an unsheared initial condition of random particle configurations, this system has evolved in time to form two plugs near the walls, with a very dilute region of particles in the bulk of the shear cell. Note that the particles are densely packed within the plugs. With the same parameter combinations, we have checked that this system also evolves to yield a single central plug, located symmetrically around

the x-axis (Tan 1995; Alam 2003). Both of these solutions satisfy the underlying symmetries of the shear flow (see § 3.1 for details) and hence are permissible. It has recently been shown, via linear stability and bifurcation analyses (Alam & Nott 1998; Nott *et al.* 1999), that such plugged solutions in the plane Couette flow are indeed picked up by the kinetic-theory-based hydrodynamic equations. The standard Navier–Stokes-level Newtonian hydrodynamics, thus, appears to be the minimal rheological model that is required to describe the dynamics of such rapid granular flows.

Returning to figure 1, we note that these non-uniform structures are reminiscent of shear-band formation in dense (slow) granular flows and suspensions (e.g. in wormlike micelles undergoing shear and many other complex fluids, see Olmsted & Lu 1997; for a review on related issues, see Goddard & Alam 1999). Of course, gravity destroys the underlying symmetry of the plane Couette flow, but with gravitational acceleration close to zero the analogues of structures in figure 1, with 'floating' plugs near the top wall or located somewhere within the Couette cell, would still survive. At the other extreme of slow flows with very low shear rates, the molecular dynamics simulations of gravitational Couette flow (Thompson & Grest 1991; Zhang & Campbell 1992) suggest that an intense shearing layer near the top wall coexists with a dense unsheared plug near the bottom wall as in the classic case of shear localization in shear-cell experiments.

Since the non-uniform structures of the type in shown figure 1 are also solutions of the associated continuum equations for rapid flows (Nott *et al.* 1999), it is natural to ask what the role of gravity would be in the fate of such solutions as we move from microgravity conditions towards the Earth-bound shear-cell experiments where gravitational effects are likely to dominate. Is there any connection between these non-uniform solutions in the rapid flow regime and the shear-banding solutions in the slow regime? Can we explain shear-band formation in dense granular flows from the associated hydrodynamic equations of rapid flows? These are the questions that we have addressed in this paper by systematically examining the role of gravity in the plane Couette flow of a granular material.

This paper is organized as follows. In § 2 we briefly outline the kinetic-theory-based hydrodynamic model, along with boundary conditions and formulate the related stability problem. In § 3.1 we consider the instability of the uniform shear flow to layering disturbances (having no variations in the streamwise direction), and briefly describe the properties of the associated shear-banding-type instability (Alam & Nott 1998). These instabilities give birth to new steady solutions having variations in the transverse direction only, leading to alternating bands of dense and dilute regions (similar to shear-band patterns in dense granular Couette flows). In § 3.2 a typical bifurcation diagram for the uniform shear flow is described, showing how different solutions bifurcate from the uniform-shear state. This is followed by a description of the role of gravity in the fate of these bifurcating solutions. The stability of these plugged states and the role of gravity are discussed in § 4. The possible effects of boundary conditions on the plugged states and their instability patterns are discussed in § 5. The conclusions are provided in § 6.

2. Governing equations and boundary conditions

We consider a granular material, consisting of monodisperse particles of diameter $\tilde{d}$ and mass density $\tilde{\rho}$, bounded by two solid plane walls at $\tilde{y} = -\tilde{H}/2$ and $\tilde{H}/2$; the gravitational acceleration $\tilde{g}$ is acting in the negative y-direction. (In the following, quantities with a tilde are dimensional and the corresponding ones without represent

their non-dimensional counterparts.) The upper wall moves with a velocity $\tilde{u}_w/2$ in the $\tilde{x}$-direction and the lower wall moves with the same velocity in the opposite direction. As in Alam & Nott (1998), we use the kinetic-theory rheological model of Lun *et al.* (1984). The non-dimensional balance equations for mass, momentum and granular energy are

$$\frac{\mathrm{D}\nu}{\mathrm{D}t} = -\nu\nabla\cdot\boldsymbol{u}, \tag{2.1}$$

$$\nu\frac{\mathrm{D}\boldsymbol{u}}{\mathrm{D}t} = -\frac{\nu H}{Fr^2}\boldsymbol{i}_y - \frac{1}{H^2}\nabla p + \frac{1}{H^2}\nabla\cdot[\mu(\nabla\boldsymbol{u}+\nabla\boldsymbol{u}^T)+\lambda(\nabla\cdot\boldsymbol{u})\boldsymbol{I}], \tag{2.2}$$

$$\begin{aligned}\tfrac{3}{2}\nu\frac{\mathrm{D}T}{\mathrm{D}t} = {} & \frac{1}{H^2}\nabla\cdot(\kappa\nabla T+\kappa_h\nabla\nu) - p(\nabla\cdot\boldsymbol{u}) \\ & + 2\mu\left[\left(\frac{\partial u}{\partial x}\right)^2+\left(\frac{\partial v}{\partial y}\right)^2+\frac{1}{2}\left(\frac{\partial u}{\partial y}+\frac{\partial v}{\partial x}\right)^2+\frac{\lambda}{2\mu}(\nabla\cdot\boldsymbol{u})^2\right] - \mathscr{D},\end{aligned} \tag{2.3}$$

where ν is the solid fraction (volume fraction of particles), $\boldsymbol{u}=(u,v)^T$ the velocity vector, T the granular temperature (i.e. fluctuating kinetic energy), $\mathrm{D}/\mathrm{D}t=\partial/\partial t+\boldsymbol{u}\cdot\nabla$ the material derivative, $H=\tilde{H}/\tilde{d}$ the non-dimensional wall separation, $Fr=\tilde{u}_w/\sqrt{\tilde{g}\tilde{d}}$ the Froude number and $\boldsymbol{i}_y$ the unit vector in y-direction. In the above, we have used the wall-to-wall gap $\tilde{H}$ as the length scale, the velocity difference between the walls $\tilde{u}_w$ as the velocity scale and the inverse of the overall shear rate $\tilde{H}/\tilde{u}_w$ as the time scale. The non-dimensional transport coefficients are

$$p(\nu,T)=f_1(\nu)T,\ \mu(\nu,T)=f_2(\nu)\sqrt{T},\ \zeta(\nu,T)=f_3(\nu)\sqrt{T},\ \lambda(\nu,T)=\left(\zeta-\frac{2}{3}\mu\right),$$
$$\kappa(\nu,T)=f_4(\nu)\sqrt{T},\ \kappa_h(\nu,T)=f_{4h}(\nu)T^{3/2}\quad\text{and}\quad\mathscr{D}(\nu,T)=f_5(\nu,e)T^{3/2}.$$

The functional forms of f_1 to f_5 are taken from Lun *et al.* (1984), and are written down explicitly in Alam & Nott (1998).

With the above non-dimensionalization, the top wall moves with a velocity $1/2$ and the bottom wall with $-1/2$. There are four control parameters in this problem: the coefficient of restitution e, the average solid fraction $\overline{\nu}$, the non-dimensional Couette gap H, and the Froude number Fr. Note that Fr can be expressed as a ratio between two time scales

$$Fr=\frac{\tilde{H}/\sqrt{\tilde{g}\tilde{d}}}{\tilde{H}/\tilde{u}_w}=\tilde{\gamma}\tilde{\tau}_d, \tag{2.4}$$

where $\tilde{\gamma}=\tilde{H}/\tilde{u}_w$ is the imposed shear rate, representing an external macroscopic time scale, and $\tilde{\tau}_d=H(\tilde{d}/\tilde{g})^{1/2}$ is the gravitational time scale. We can get back the gravity-free case ($Fr=\infty$) by considering the infinite shear-rate limit. Thus, under the present formulation, increasing gravitational effects correspond to decreasing either the value of Fr or the shear rate γ (with other parameters being fixed). Note further that the terminologies 'solid fraction' and 'density' will interchangeably be used to refer to the same quantity ν.

The boundary conditions for granular fluids differ from those of Newtonian fluids in the possibility of slip at the walls and the associated energy generation along with energy loss (dissipation) due to inelastic particle–wall collisions (Jenkins & Richman 1986; Johnson & Jackson 1987). By equating the tangential stress in the bulk adjacent to the boundary with the tangential momentum flux due to wall–particle collisions,

the boundary condition for the slip velocity can be obtained as

$$\frac{\boldsymbol{u}_s}{|\boldsymbol{u}_s|} \cdot \boldsymbol{\Sigma} \cdot \boldsymbol{n} = H\,|\boldsymbol{S}^w|. \tag{2.5}$$

Here $\boldsymbol{\Sigma}$ is the bulk stress tensor, $\boldsymbol{S}^w$ is the tangential momentum flux, $\boldsymbol{n}$ the unit normal from the wall directed into the particle assembly, and $\boldsymbol{u}_s = \boldsymbol{u} - \boldsymbol{u}_w$ the slip velocity, with $\boldsymbol{u}$ being the velocity of the granular material in contact with the wall and $\boldsymbol{u}_w$ the wall velocity. Equating the flux of the granular energy ($\boldsymbol{q}$) normal to the wall to its net production at the wall (due to the slip velocity) yields the following boundary condition on granular temperature:

$$\boldsymbol{n} \cdot \boldsymbol{q} = H^3 \boldsymbol{u}_s \cdot \boldsymbol{S}^w - H\,\mathscr{D}^w. \tag{2.6}$$

Simple functional forms of the tangential momentum flux, $\boldsymbol{S}^w$, and the dissipation rate per unit area, $\mathscr{D}^w$, are taken from Johnson & Jackson (1987):

$$\boldsymbol{S}^w = \frac{\phi\sqrt{3}\pi\nu\chi(\nu)\sqrt{T}\,\boldsymbol{u}_s}{6\nu_{max}} \quad \text{and} \quad \mathscr{D}^w = \frac{\sqrt{3}\pi\nu\chi(\nu)T^{3/2}\left(1-e_w^2\right)}{4\nu_{max}}.$$

Here ϕ is the specularity coefficient which is a measure of the roughness of the wall, and its value varies between zero for perfectly specular collisions (i.e. a smooth wall) and unity for perfectly diffuse collisions (i.e. a rough wall); e_w is the coefficient of restitution for particle–wall collisions. The function $\chi(\nu)$ is the radial distribution function at contact

$$\chi(\nu) = \frac{1}{1-(\nu/\nu_{max})^{1/3}}$$

that diverges at $\nu = \nu_{max}$, the maximum solid fraction, which is chosen to be 0.65, representing the random close packing limit, as in the previous work (Alam & Nott 1998). Choosing a different value for ν_{max} (≈ 0.906 in two dimensions) or a different functional form for $\chi(\nu)$ (for example, the Carnahan–Starling equation) would not change our results qualitatively. When the production term in (2.6) exceeds the collisional dissipation term, there is a net flow of energy from the wall to the bulk, i.e. the wall acts as a source of granular energy. On the other hand, the wall acts as a sink of granular energy if the collisional energy dissipation exceeds its production in (2.6). For the bulk of the results presented below, the usual no-slip and zero-heat-flux boundary conditions will be used, and the effects of wall slip and non-adiabaticity are discussed in § 5.

2.1. *Base flow and stability*

Now we formulate the stability problem for the plane Couette flow and the associated base state. For the steady ($\partial/\partial t = 0$), fully developed ($\partial/\partial x = 0$) flow, the continuity equation is identically satisfied, and the momentum and energy balances take the following form:

$$\left.\begin{aligned} \frac{\mathrm{d}}{\mathrm{d}y}\left(\mu\frac{\mathrm{d}u}{\mathrm{d}y}\right) = 0, \qquad \frac{\mathrm{d}p}{\mathrm{d}y} + \frac{\nu H^3}{Fr^2} = 0, \\ H^{-2}\frac{\mathrm{d}}{\mathrm{d}y}\left(\kappa\frac{\mathrm{d}T}{\mathrm{d}y} + \kappa_h\frac{\mathrm{d}\nu}{\mathrm{d}y}\right) + \mu\left(\frac{\mathrm{d}u}{\mathrm{d}y}\right)^2 - \mathscr{D} = 0. \end{aligned}\right\} \tag{2.7}$$

We will analyse the stability of the solution $[\nu(y), u(y), T(y)]$ of these equations with appropriate boundary conditions.

To investigate stability, the base flow is perturbed by infinitesimal disturbances (e.g. $\nu(x, y, t) = \nu(y) + \nu'(x, y, t)$, etc.), and their time evolution is studied by linearizing the equations of motion around the solution of (2.7). The linearized disturbance equations can be written in operator form as

$$\frac{\partial X}{\partial t} = \mathscr{L} X, \quad \text{with} \quad \mathscr{B}^{\pm} X = 0 \quad \text{at} \quad y = \pm 1/2, \tag{2.8}$$

with $X = (\nu', u', v', T')$ being the eigenfunction. The explicit forms of the linear stability operator $\mathscr{L}(\cdot)$ and the boundary operators $\mathscr{B}^{\pm}(\cdot)$ are omitted for the sake of brevity. Since the disturbance equations and the boundary conditions are invariant under translation in x, we could seek solutions via the standard Fourier decomposition:

$$[\nu', u', v', T'](x, y, t) = [\hat{\nu}, \hat{u}, \hat{v}, \hat{T}](y)\, \mathrm{e}^{\mathrm{i}k_x x + \omega t}, \tag{2.9}$$

where the quantities with hats are complex amplitude functions of y, and k_x is the wavenumber in the streamwise direction. As in the temporal stability problem (Drazin & Reid 1985), k_x is assumed to be real and $\omega = \omega_r + \mathrm{i}\omega_i$ is the complex frequency: ω_r determines the rate of growth/decay of disturbances and ω_i is the frequency of the disturbance. The flow is stable/unstable for $\omega_r < 0$, or > 0, respectively, and neutrally stable for $\omega_r = 0$.

3. Instability, bifurcation and the ordering phenomenon

3.1. *Instability of the uniform shear flow: layering instability*

In order to explicitly show the connection between the instability-induced ordering phenomenon in uniform shear flow and the shear-band formation in gravitational Couette flow, we first focus on the gravity-free case ($Fr = \infty$) of steady, fully developed flow, with no-slip ($\boldsymbol{u}_s = 0$) and zero heat-flux ($\boldsymbol{n} \cdot \boldsymbol{q} = 0$) boundary conditions. Walls with these boundary conditions will henceforth be called adiabatic walls, and non-adiabatic walls otherwise.

The idealized boundary conditions of adiabatic walls admit a uniform shear solution with constant solid fraction and granular temperature:

$$\nu(y) = \text{const.} = \overline{\nu}, \quad u(y) = y, \quad T(y) = \frac{f_2(\nu)}{f_5(\nu, e)}, \tag{3.1}$$

having the centre-symmetry

$$[\nu, u, T](y) = [\nu, -u, T](-y), \tag{3.2}$$

i.e. the solid fraction and granular temperature are symmetric about the centreline ($y = 0$) and the streamwise velocity is antisymmteric about $y = 0$. It can be verified that the linearized disturbance equations for the uniform shear case remain invariant under the transformation

$$(x, y) \to (-x, -y), \quad \omega \to \omega, \quad [\hat{\nu}, \hat{u}, \hat{v}, \hat{T}] \to [\hat{\nu}, -\hat{u}, -\hat{v}, \hat{T}]. \tag{3.3}$$

This simply implies that if $\mathrm{e}^{\mathrm{i}k_x x}[\hat{\nu}, \hat{u}, \hat{v}, \hat{T}](y)$ is an eigenmode of the stability equations with eigenvalue ω, then $\mathrm{e}^{-\mathrm{i}k_x x}[\hat{\nu}, -\hat{u}, -\hat{v}, \hat{T}](-y)$ is also an eigenmode with eigenvalue ω. In other words, there are conjugate pairs of modes with the same growth rate but having positive and negative phase velocities (i.e. forward and backward propagating modes). This is a consequence of the centre-symmetry (3.2) of the uniform shear flow. Note that the inclusion of gravity will destroy this symmetry, and we shall discuss this issue again in § 3.2.

It is known that the uniform shear flow is unstable to a multitudes of disturbances, leading to both stationary and travelling wave patterns (Alam & Nott 1998). Here we focus only on a special kind of instability that arises due to purely streamwise disturbances ($k_x = 0$) which give birth to alternating layered bands of dilute and dense regions in the transverse direction (Wang, Jackson & Sundaresan 1996; see also Nott *et al.* 1999). For such layering modes, the linearized disturbance equations (2.8) admit analytical solutions with the eigenfunctions being given in terms of sine and cosine functions (Alam & Nott 1998):

$$\left.\begin{aligned} \hat{v}(y) &= \hat{v}_1 \cos n\pi\left(y \pm \tfrac{1}{2}\right), \quad \hat{T}(y) = \hat{T}_1 \cos n\pi\left(y \pm \tfrac{1}{2}\right), \\ \hat{u}(y) &= \hat{u}_1 \sin n\pi\left(y \pm \tfrac{1}{2}\right), \quad \hat{v}(y) = \hat{v}_1 \sin n\pi\left(y \pm \tfrac{1}{2}\right), \end{aligned}\right\} \tag{3.4}$$

where the mode number n is a positive integer. Substitution of (3.4) into the linearized disturbance equations results in a quartic dispersion relation for ω:

$$\omega^4 + a_3\omega^3 + a_2\omega^2 + a_1\omega + a_0 = 0. \tag{3.5}$$

An asymptotic analysis of this dispersion relation for large H shows that the unstable mode is one of the real roots of (3.5) and hence the instability is stationary (Alam 1998*a*). Thus, the locus of neutral stability is obtained by simply setting $\omega = 0$ in (3.5):

$$H(\nu, e) = n\pi\sqrt{\frac{N_1}{N_2}} \sim (1 - e^2)^{-1/2} \tag{3.6}$$

where

$$N_1(\nu, e) = \frac{1}{f_5}\left[f_4 - f_{4h} f_1 \left(\frac{\mathrm{d}f_1}{\mathrm{d}\nu}\right)^{-1}\right],$$

$$N_2(\nu, e) = f_1 \left(\frac{\mathrm{d}f_1}{\mathrm{d}\nu}\right)^{-1} \left[\frac{1}{f_5}\left(\frac{\mathrm{d}f_5}{\mathrm{d}\nu}\right) + \frac{1}{f_2}\left(\frac{\mathrm{d}f_2}{\mathrm{d}\nu}\right)\right] - 2.$$

It is clear from (3.6) that the $n = 1$ mode is the first to become unstable as H increases at a fixed $\overline{\nu}$, and the onset of this instability represents the neutral stability contour in the (H, $\overline{\nu}$)-plane which can be calculated from (3.6) by specifying a value for the restitution coefficient e. Thus, the flow is stable to layering modes when the Couette gap is sufficiently small; as H exceeds a critical value H_c, which is a function of $\overline{\nu}$ and e, the flow becomes unstable. Beyond $H > H_c$, the successive higher-order modes ($n = 2, 3, \ldots$) take over as the most unstable mode at $H = nH_c$. There is also a minimum value of solid fraction ($\overline{\nu}_{min} \sim 0.15$), which is a weak function of e, below which the flow remains stable (Alam & Nott 1998).

3.2. *Bifurcation from uniform shear flow and the role of gravity: universal unfoldings and isolas*

Treating the Couette gap H as a control parameter, there is now a countably infinite number of bifurcation points located at $H = nH_c$ for $\overline{\nu} > \overline{\nu}_{min}$. From each of these bifurcation points, new solutions are born as a result of the nonlinear saturation of the associated infinitesimal instability (Nott *et al.* 1999). These nonlinear bifurcating solutions are nothing but the solutions of the reduced set of equations (2.7), which are computed numerically by using the fourth-order Runga–Kutta method along with a numerical continuation scheme.

Let us now look at the bifurcation scenerio from the uniform shear solution. (Note that all the results presented in this section correspond to adabatic walls, i.e. with

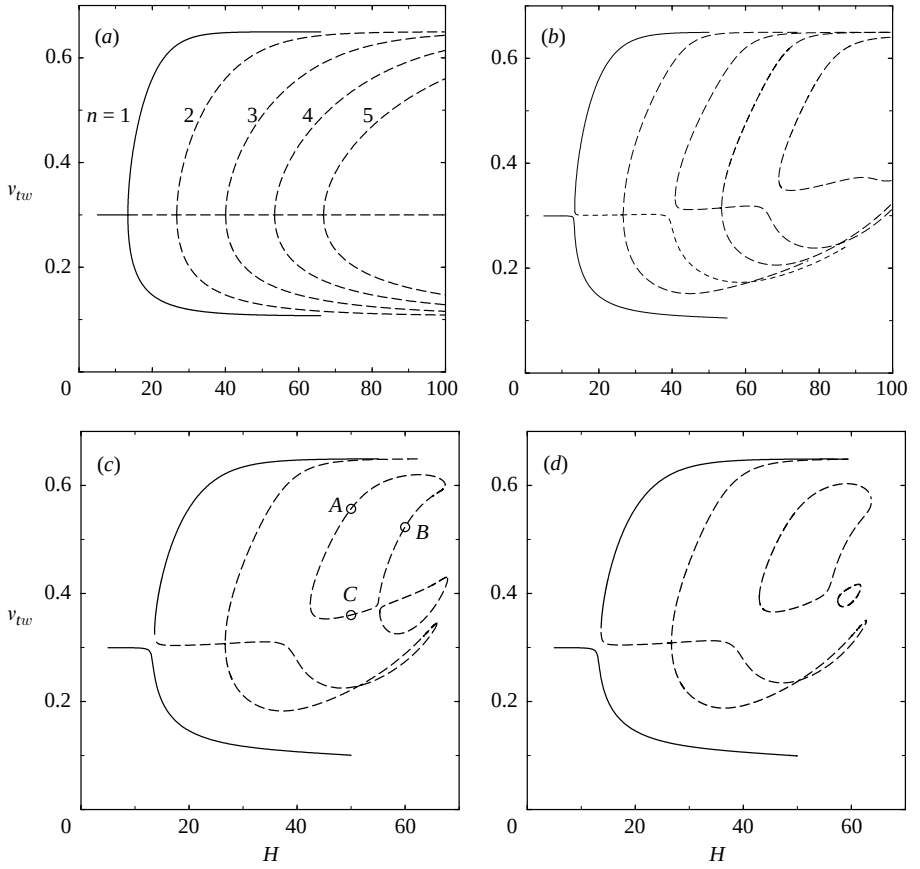

FIGURE 2(*a–d*). For caption see facing page.

no-slip and zero-heat-flux boundary conditions.) Figure 2(a) shows a typical bifurcation diagram for the uniform shear case in the (H, ν_{tw})-plane with the parameter values set to $\overline{\nu} = 0.3$ and $e = 0.8$. Here $\nu_{tw} = \nu(1/2)$, the value of the solid fraction at the top wall, is treated as the order parameter and the Couette gap H as the bifurcation parameter (see the Appendix for related definitions). The horizontal line refers to uniform shear, for which the density is uniform across the Couette gap, and hence the value of the order parameter ν_{tw} is simply $\overline{\nu}$. As the bifurcation parameter H is increased, the uniform shear flow loses stability to the first layering mode ($n = 1$) at $H = H_c \approx 13.27$, giving birth to two stable solution branches. Note that the bifurcation is of pitchfork-type (since the least-stable eigenvalue is real) and supercritical in nature. (In the language of phase transitions, the supercritical bifurcation corresponds to a second-order or continuous phase transition.) Near the bifurcation point the order parameter ν_{tw} differs from $\overline{\nu}$, suggesting that the flow develops a density inhomogeneity across the Couette gap, and the degree of this inhomogeneity ($=\nu_{tw} - \overline{\nu}$) becomes pronounced as we move away from the bifurcation point. With further increase in $H > H_c$, other modes lose stability progressively, giving birth to additional bifurcation branches (the first five bifurcation points are shown in figure 2*a*). As in the case of the first mode, two solution branches emanate from each bifurcation point, and such pairs of solutions arise due to the underlying symmetry of the uniform shear flow (3.2) and (3.3). Note that all the upper bifurcation branches

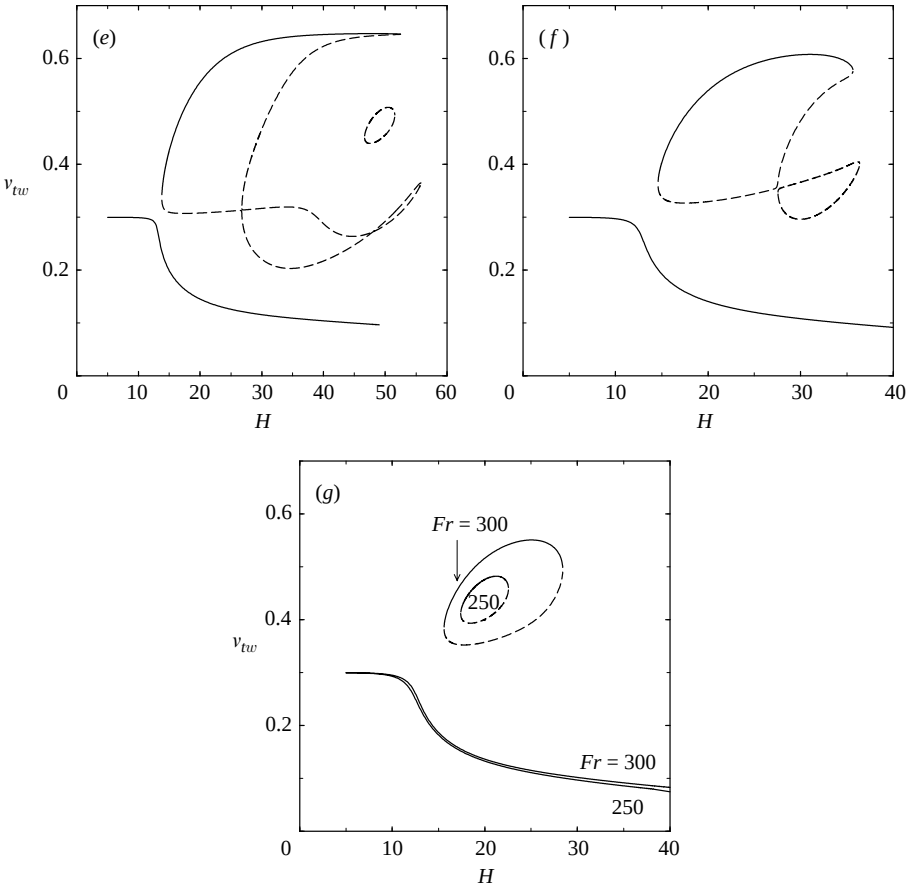

FIGURE 2. Bifurcation diagrams in the (H, ν_{tw})-plane, with $\nu_{tw} \equiv \nu(1/2)$ being the value of the solid fraction at the top wall, for various values of the Froude number: (*a*) $Fr = \infty$, (*b*) 2000, (*c*) 1000, (*d*) 922, (*e*) $Fr = 750$, (*f*) 400, (*g*) 300 and 250. The average solid fraction is $\overline{\nu} = 0.3$, and the coefficient of restitution is $e = 0.8$. The no-slip and zero-heat-flux boundary conditions have been imposed. The solid and dashed lines represent stable and unstable solutions, respectively.

asymptote to $\nu_{tw} \to 0.65 = \nu_{max}$, which corresponds to the maximum allowable solid fraction in the system, representing the random close-packing limit, as mentioned before.

To clarify the structure of bifurcating solutions, we briefly recall their symmetries about the centreline ($y = 0$). The solutions emerging from $H = H_c, 3H_c, \ldots$ are asymmetric, having no symmetry about the centreline, since the eigenfunctions for odd modes ($n = 1, 3, \ldots$),

$$\left.\begin{array}{ll} \hat{v}(y) = -\hat{v}(-y), & \hat{T}(y) = -\hat{T}(-y), \\ \hat{u}(y) = \hat{u}(-y), & \hat{v}(y) = \hat{v}(-y). \end{array}\right\} \tag{3.7}$$

destroy the centre-symmetry (3.2) of uniform shear. For example, the solutions corresponding to the first mode ($n = 1$) have density maxima/minima near either of the walls (see figures 14 and 15 of Nott *et al.* 1999). It is worth pointing out that such asymmetric solution profiles with plugs near the top/bottom wall were subsequently verified in particle dynamics simulations of plane Couette flow (Sasvari, Kertesz & Wolf 2000). On the other hand, the solutions from $H = 2H_c, 4H_c, \ldots$

preserve (3.2), since the eigenfunctions for even modes ($n = 2, 4, \ldots$) satisfy

$$\left.\begin{aligned} \hat{\nu}(y) &= \hat{\nu}(-y), & \hat{T}(y) &= \hat{T}(-y), \\ \hat{u}(y) &= -\hat{u}(-y), & \hat{v}(y) &= -\hat{v}(-y). \end{aligned}\right\} \tag{3.8}$$

The resulting bifurcating solutions for density, temperature and velocity thus satisfy the centre-symmetry (3.2), and will henceforth be called symmetric solutions (see, for example, figure 1 which corresponds to $n = 2$ mode).

Figure 2(*b–g*) displays a series of bifurcation diagrams in the (H, ν_{tw})-plane for various values of Fr, showing the effect of gravity on the topology of bifurcations. The parameter values are as in the uniform shear case 2(*a*). At $Fr = 2000$ (panel *b*), there is already a qualitative change in the bifurcation diagram in that the solution branches from the odd modes ($n = 1$, 3 and 5) have peeled off from the uniform shear solution. Each of the three corresponding bifurcation points (for the gravity-free case) has transformed into a turning point (i.e. saddle-node bifurcation), via merging with the adjacent uniform-shear branch, and a smooth solution branch. This is a signature of imperfect bifurcation (Golubitsky & Schaeffer 1985; Nott *et al.* 1999), which is also known as the unfolding of bifurcations in the realm of singularity theory (see the Appendix for related details). Thus, *gravity acts as an imperfection in the present problem*, destroying the 'perfect' bifurcation structure of the gravity-free case (Alam 1998*b*, 2004*a*). Note further in figure 2(*b*) that the separation between two successive turning points is larger at higher H, clearly suggesting that the higher-order branches start peeling off first. This is due to the fact that for a given Fr the degree of imperfection ($\propto H^3/Fr^2$, see equation (2.7)) increases with increasing H. Hence in a typical bifurcation diagram in the (H, ν_{tw})-plane, as in figure 2, the signature of imperfection will first be observed at $H = \infty$ for an arbitrarily small value of Fr^{-1}.

As we decrease the Froude number to $Fr = 1000$ (panel *c*), the solution branches from the even mode $n = 4$ are observed to peel off, leading to the formation of two distinct isolas via merging between two successive odd and even bifurcation branches. (An 'isola' is defined as a closed solution curve in the bifurcation diagram; see the Appendix.) Interestingly, the size of each isola has decreased as the Froude number is decreased to $Fr = 900$ (panel *d*). The righmost isola in panel (*d*) vanishes altogether at $Fr = 750$ as observed in (*e*), and the size of the other isola in (*d*) has become even smaller at $Fr = 750$, which eventually vanishes at $Fr \approx 700$. Essentially the two turning points of each isola coalesce to form an isola centre at some critical value of Fr, below which the gravity does not permit the associated solutions.

Before proceeding to discuss other features of bifurcation diagrams, let us try to clarify the solution structure associated with the isolas in figure 2. Figure 3(*a–c*) shows the variations of density, granular temperature and velocity at three points A, B and C on the left isola in figure 2(*c*). All three profiles in each panel look vastly different from each other, suggesting their different origin (gravity-free case). The profiles at C appear to be modulated versions of their uniform-shear counterparts. Comparing the density profiles at A and B with those for the gravity-free case (not shown here for the sake of brevity) we find that each pair has similar structural features (i.e. the number of local density maxima, etc.) and hence they are related. Thus we conclude that the left isola in figure 2(*c*) has evolved by combining three solution branches of the gravity-free case, namely the upper branches of $n = 3, 4$ and the adjoining unform-shear branch.

From the sequence of bifurcation diagrams as in figure 2, we have ascertained that the isolas are formed sequentially in pairs, and the kth and $(k + 1)$th isolas combine

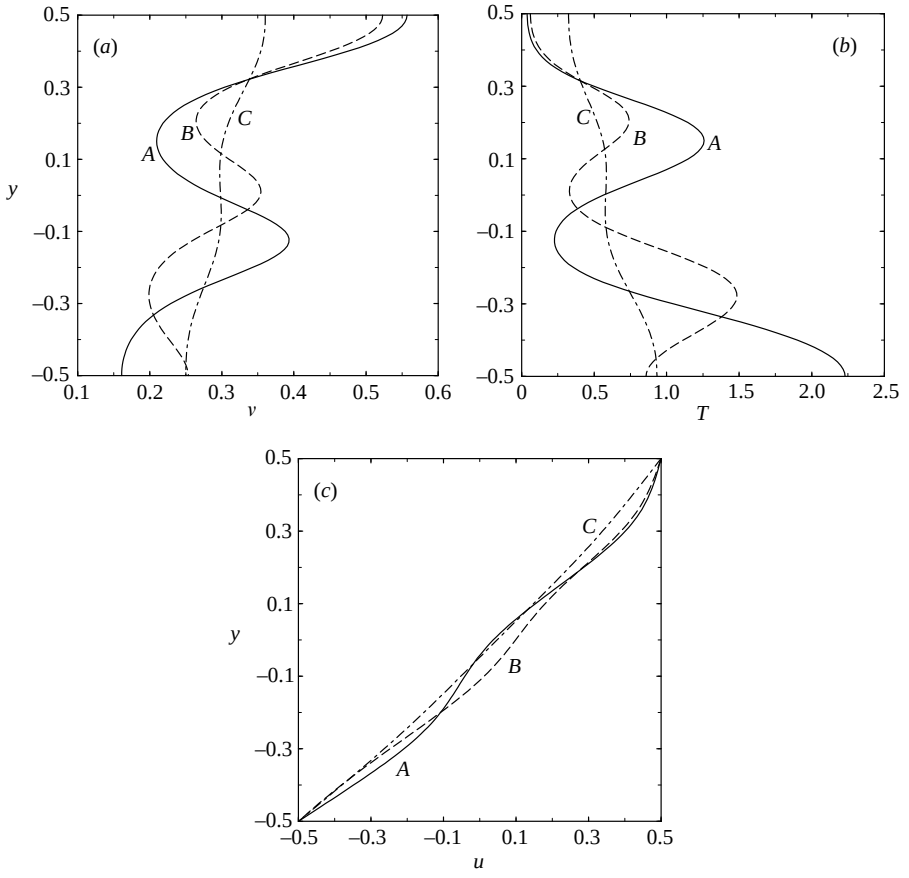

FIGURE 3. Comparison of (*a*) solid fraction, (*b*) granular temperature and (*c*) velocity profiles at three points *A* ($H = 50$), *B* ($H = 60$) and *C* ($H = 50$), located on the left isola in figure 2(*c*).

the following solution branches:

$$k^u + 0 + (k+1)^u \quad \text{and} \quad (k+1)^l + 0 + (k+2)^l,$$

with the superscripts u and l referring to the upper and lower bifurcation branches, respectively, and 0 denoting the adjoining uniform-shear branch between the two successive bifurcation branches. (Recall that the lower branch of the first pair of bifurcation branches does not take part in isola formation.) In fact, a countably infinite number of such pairs of isolas are born, shrink in size and subsequently die (with the last isola, i.e. the one at $H = \infty$, dying first and so on) as the shear rate decreases from infinity ($Fr = \infty$). This sequence of birth and death of isolas continues on decreasing the value of Fr (i.e. the gravitational effects are increasing) as observed in figures (*f*) and 2(*g*). At a low enough value of Fr ($\sim$240), the only possible solution branch that survives in figure 2 is the lower branch of the first mode ($n = 1$) which extends up to $H = \infty$. Note that the density profile corresponding to this 'unique' solution branch has a plug near the bottom wall.

From here onwards we will focus on the first pair ($n = 1$) of solution branches in figure 2 since they are stable and one of them survives at all shear rates. To understand the effect of gravity on the solution structure of these two branches, we

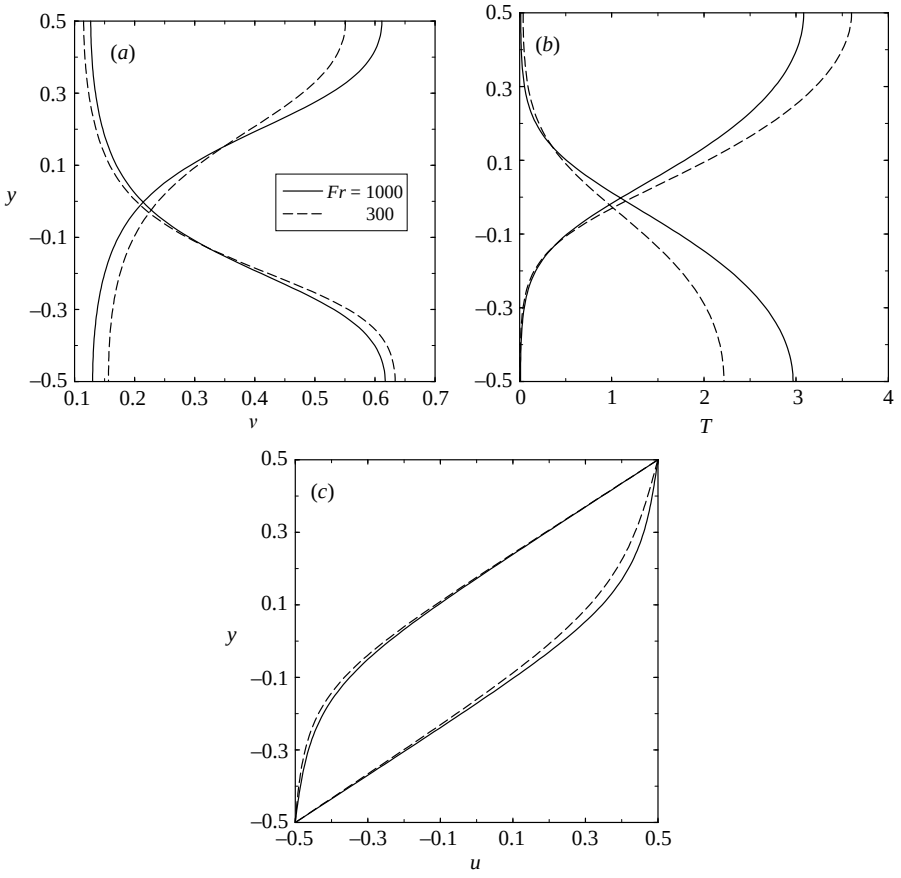

FIGURE 4. Effect of gravity (i.e. Froude number Fr) on the variations of (a) solid fraction, (b) granular temperature and (c) streamwise velocity across the Couette gap for the first pair ($n=1$) of solution branches in figure 2: $\overline{\nu}=0.3$, $e=0.8$ and $H=25$.

show the profiles of density, temperature and velocity in figure 4(a–c). The solid and dashed lines represent solutions at $Fr=1000$ and 300, respectively; the Couette gap is set to $H=25$, with other parameters as in figure 2. The corresponding profiles for the gravity-free case ($Fr=\infty$) differ very little from those at $Fr=1000$, and hence are not displayed. It is observed from panel (a) that the plug near the bottom/top wall compacts/decompacts as the Froude number Fr decreases (i.e. the gravitational effects are increasing). Looking at the solution profiles with a plug near the bottom wall, we find that such compaction clearly leads to a lower temperature as seen in panel (b), and a relatively lower shear rate within the plug as in panel (c). Similarly, the top plug decompacts with decreasing Fr, resulting in increased temperature and shear rate within the plug. For the plane Couette flow with gravity, the pressure is non-uniform across the Couette gap and the gradient of this dispersive pressure is balanced by an effective gravitational potential as in (2.7). This is responsible for compaction or decompaction of the plug as we decrease the value of Fr from ∞, depending on whether the plug is located near the bottom or top wall, respectively.

Next we consider the bifurcation structure for dense flows ($\overline{\nu}=0.5$) in figure 5 which displays a series of bifurcation diagrams for different values of Fr, with other

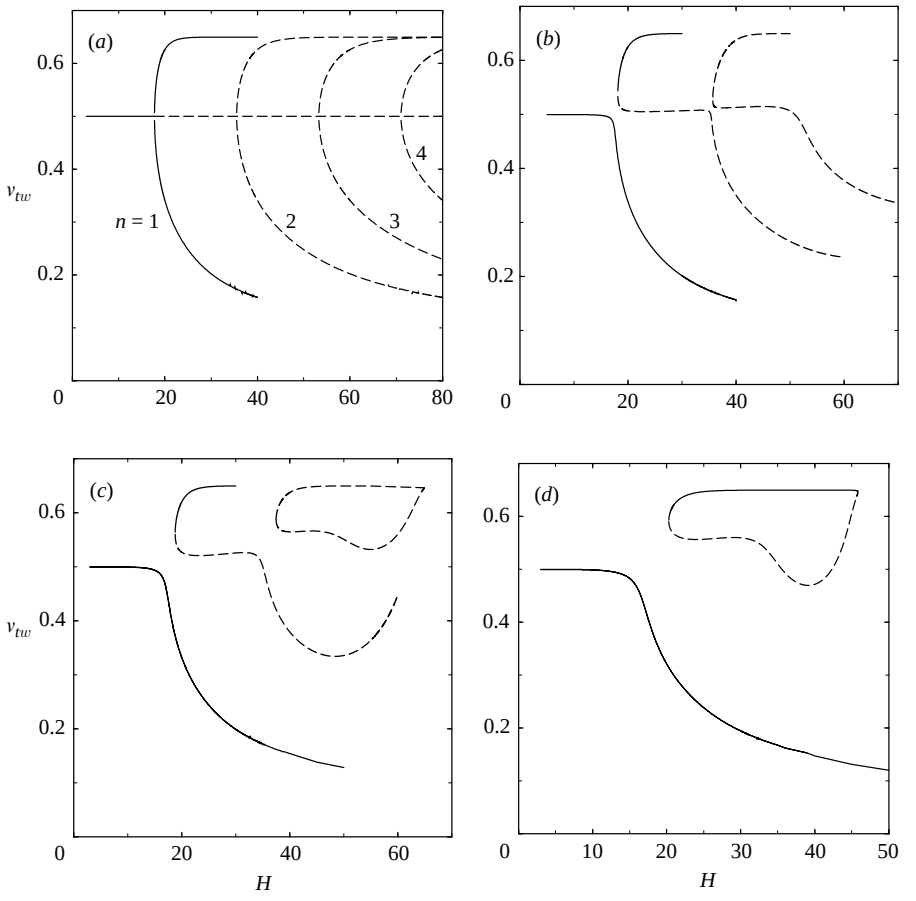

FIGURE 5. Bifurcation diagrams in the (H, v_{tw})-plane for dense flows ($\overline{\nu} = 0.5$): (*a*) $Fr = \infty$, (*b*) 1000, (*c*) 500, (*d*) 300. Other parameters are as in figure 2. The solid and dashed lines represent stable and unstable solutions, respectively.

parameters as in figure 2. As in the case of $\overline{\nu} = 0.3$, the overall features (e.g. the onset of saddle-node bifurcations, the formation of isolas, etc.) remain similar. However, the topology of isola formation for dense flows appears to be different than that at $\overline{\nu} = 0.3$. It is clear from figure 5 that the isolas are now born one-by-one as Fr decreases, by combining two successive upper and lower bifurcation branches (in contrast to two successive upper/lower branches at $\overline{\nu} = 0.3$) via the adjoining uniform-shear branch. For example, the kth isola combines the following solution branches:

$$k^u + 0 + (k+1)^l,$$

with the superscripts u and l referring to upper and lower branches. Of course, a countably infinite number of such isolas are again born, dying subsequently as Fr decreases from infinity. Here also, the solution at low shear rates is the one with a plug near the bottom wall, corresponding to the lower branch of the first pair of bifurcation branches. The comparison of density, granular temperature and velocity, for this stable solution branch, at different Fr (=300 and 1000) is shown figure 6(*a–c*). The Couette gap is $H = 25$, with other parameters as in figure 5. As in the moderate density case (cf. figure 4), the increasing gravitational effects lead to compaction/decompaction of the plug (see panel *a*), depending whether the plug

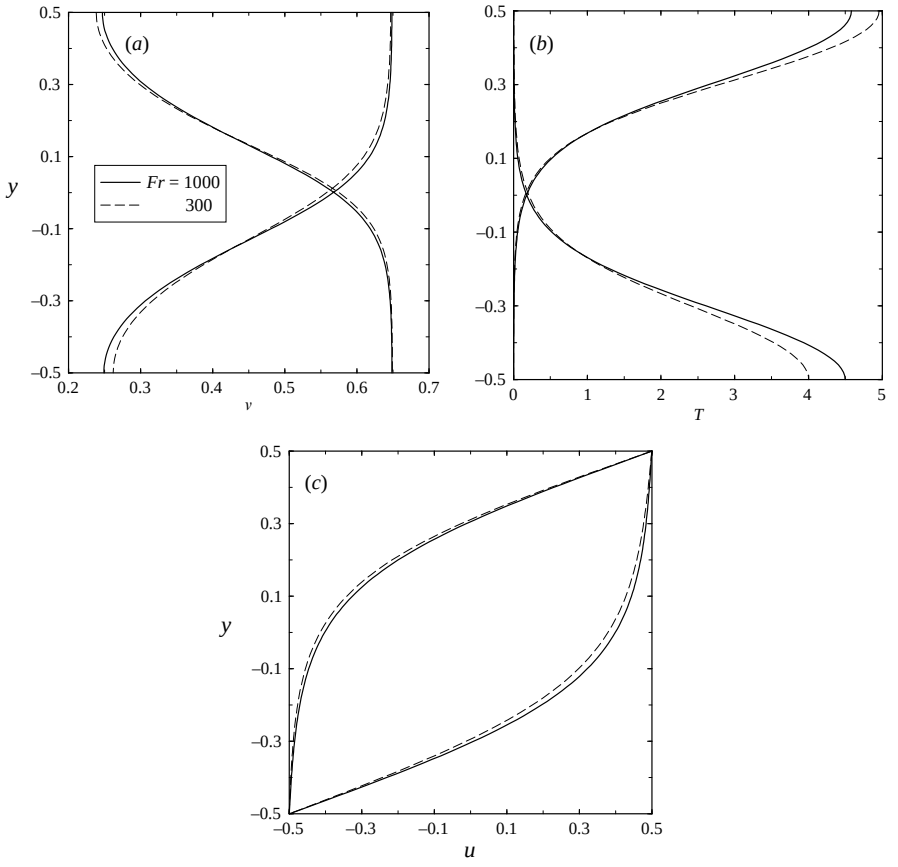

FIGURE 6. Effect of gravity on the variations of (*a*) solid fraction (*b*) granular temperature and (*c*) streamwise velocity across the Couette gap for the first pair ($n = 1$) of solution branches in figure 5: $\overline{\nu} = 0.5$, $e = 0.8$ and $H = 25$.

is located near the bottom/top wall, respectively. The effects of Fr on the granular temperature and velocity follow corresponding trends as seen in panels (*b*) and (*c*). In contrast to the case at $\overline{\nu} = 0.3$, the width of the plug has increased, and the width of the shear layer with almost uniform shear rate has decreased; both are consequences of the increased mean density. By further increasing the value of $\overline{\nu}$ (say, to 0.6), the topological features of the bifurcation diagram and the overall solution structure remain similar.

The general problem of imperfect bifurcation is addressed by using the theory of *universal unfolding* (Golubitsky & Schaeffer 1985) in the realm of singularity theory. Now we pause to discuss the connection of our bifurcation results with the universal unfolding of bifurcations. That the bifurcation in granular Couette flow can also be of subcritical nature has been discussed in detail by Nott *et al.* (1999); it occurs at much lower mean densities ($\overline{\nu} < 0.2$, see their figures 6*e* and 6*f*). (In the language of phase transitions, the subcritical bifurcation corresponds to a first-order or discontinuous phase transition.) The effect of gravity on such subcritical bifurcations is similar to the case at $\overline{\nu} = 0.3$, the only difference being that the smooth branch now contains two turning points (saddle-nodes) and 'hysteresis' (see the bifurcation diagram for 'zone 3' in figure 15). Such 'hysteretic' jumps, however, disappear when the Froude

number is small; we omit the related details for the sake of brevity. Returning back to the unfolding of bifurcations, we have examined the detailed structural features of all bifurcation diagrams. The conclusion that we have drawn from our analysis in the Appendix is that the effect of gravity on plane Couette flow truely belongs to the class of the 'universal' unfolding of pitchfork bifurcations, implying that all possible forms of imperfect bifurcation scenarios can be realized in the present bifurcation problem.

For a given value of the restitution coefficient, we have found that there is a critical Froude number ($Fr_c \approx 240$ at $e = 0.8$) below which only one solution exists (having a plug near the bottom wall). The range of Fr for which this unique solution exists is much larger for nearly elastic systems ($e = 0.95$, $Fr_c \approx 470$) than for moderately dissipative systems ($e = 0.5$, $Fr_c \approx 120$). This can be understood by recalling the fact that the bifurcation points (3.6) move towards infinity in the elastic limit ($e \to 1$), and hence a purely elastic sheared system under gravity supports only the unique solution with a bottom plug for all Fr.

Returning to experimental observations, we note that in Earth-bound shear-cell experiments (Savage & Syed 1984; Johnson & Jackson 1987) the Froude number is of order 10, and this clearly precludes the emergence of solutions that have plugs near the top wall or somewhere in between the two-walls. Of course, under micro-gravity conditions that correspond to large Fr, it would be possible to observe such multiple plugs 'floating' within the Couette gap. Thus, we may conclude that *the plane Couette flow under gravity admits only one solution, having a plug near the bottom wall, at low shear rates that are typically encountered in shear-cell experiments.* We have further established that *such plug formation in gravitational Couette flows is tied to the instability-induced ordering phenomenon in the closely related uniform shear flow.*

4. Are ordered plugs stable?

While at small values of Fr (i.e. at low shear rates) there is only one plug at the bottom of the Couette device, multiple plugs, arranged parallely along the transverse direction, can coexist at large Fr (i.e. at high shear rates) if the Couette gap H is large enough. It is interesting to ask whether such floating plugs in the latter case are stable/unstable since there are realizable under microgravity conditions. Since these plugged states are stable to purely streamwise perturbations ($k_x = 0$, see §4.1 below), we have probed their stability to two-dimensional perturbations with $k_x \neq 0$ by computing the growth/decay rates of infinitesimal perturbations.

The linearized stability equations (2.8) were discretized using a staggered grid spectral collocation scheme, resulting in a matrix eigenvalue problem: $\boldsymbol{A}\Phi = \omega \boldsymbol{B}\Phi$, where ω is the eigenvalue and Φ is the discrete analogue of the eigenfunction. For details on the numerical scheme, the reader is referred to Alam & Nott (1998). The QR-algorithm (of the MATLAB software) was used to solve this generalized eigenvalue problem, and the accuracy of the numerical scheme was verified by comparison with known analytical results as detailed in Alam & Nott (1998).

For the sake of better exposition of our results, we first present stability results for the gravity-free case in §4.1, focusing on the base states corresponding to the first pair of asymmetric solutions (i.e. $n = 1$ branches in figure 2*a*). This is followed by results on the influence of gravity on their stability.

4.1. *Stability of the first pair of asymmetric solutions: gravity-free case*

Before discussing stability results, it is useful to recall the symmetry (3.3) of the linearized disturbance equations for the uniform shear case. Note that for asymmetric

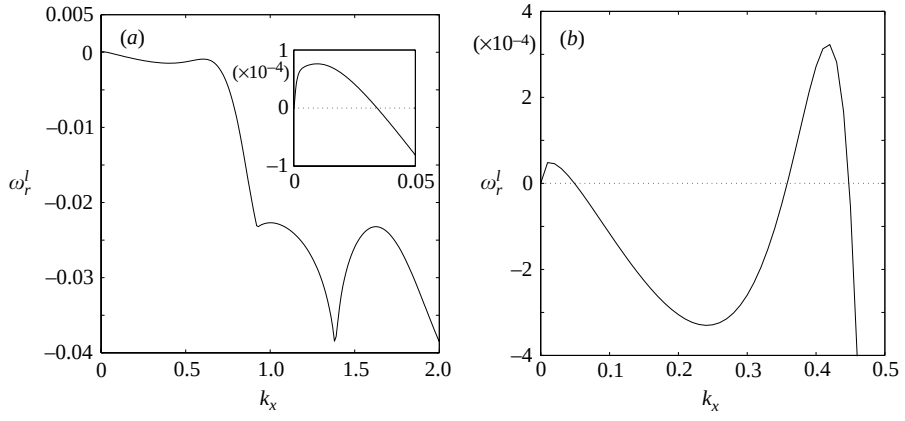

FIGURE 7. Variation of growth rate of the least stable mode with k_x. The base state corresponds to the first pair of asymmetric solutions ($n=1$) in figure 2(a) with adiabatic walls: $\overline{v}=0.3$; $e=0.8$; (a) $H=50$; (b) $H=75$.

base states, this symmetry (3.3) no longer holds, i.e. a forward-propagating mode cannot coexist with a backward-propagating mode having the same growth rate. However, we have noted in § 3.2 that such asymmetric solutions arise in pairs satisfying the following symmetry (Alam 1998):

$$v_{as}^l(y)=v_{as}^u(-y), \quad u_{as}^l(y)=-u_{as}^u(-y) \quad \text{and} \quad T_{as}^l(y)=T_{as}^u(-y), \tag{4.1}$$

with the superscripts l and u representing lower and upper bifurcation branches in figure 2(a). It immediately follows that the stability characteristics of $(v_{as}^l, u_{as}^l, T_{as}^l)$ are identical to those of $(v_{as}^u, u_{as}^u, T_{as}^u)$ except that the phase velocity of any mode of the former is just the reverse of the latter. Thus, for the gravity-free case, we need to consider the stability of one of the base states of each asymmetric pair.

Figure 7(a, b) shows the variation of the growth rate, ω_r^l, of the least stable mode with k_x at $H=50$ and $H=75$, respectively. Note that the least-stable mode is the one with the maximum growth rate among all the modes, i.e.

$$\omega_r^l = \max \omega_r.$$

The inset in panel (a) shows the long-wave modes in an expanded form. The base states correspond to the first pair of asymmetric solutions in figure 2(a), with $\overline{v}=0.3$ and $e=0.8$. It is observed that $\omega_r^l=0$ at $k_x=0$, but the growth rate increases from zero and remains positive for a small range of wavenumbers k_x. This implies that the corresponding base flow (with a plug near the top/bottom wall) is neutrally stable to layering disturbances and unstable to long-wave modes. We have checked that the dominant instability at $H=50$ is a forward travelling mode. (Following Alam & Nott 1998, we call the 'dominant' instability mode the one having the largest growth rate over all k_x.) On increasing H to 75, a second peak rises above the zero-growth-rate line (see panel b), and the dominant instability, still a forward travelling mode, is now due to this peak. The phase velocities of all unstable modes are found to be approximately 0.5.

Figure 8 shows the growth-rate contours of the least-stable mode (ω_r^l) in the (H, k_x)-plane at $\overline{v}=0.3$ and $e=0.8$. The contour with $\omega_r^l=0$, known as the neutral contour, separates the stable and unstable regions. The flow is unstable to non-layering disturbances ($k_x \neq 0$) inside the neutral contour. The unstable zones for long waves

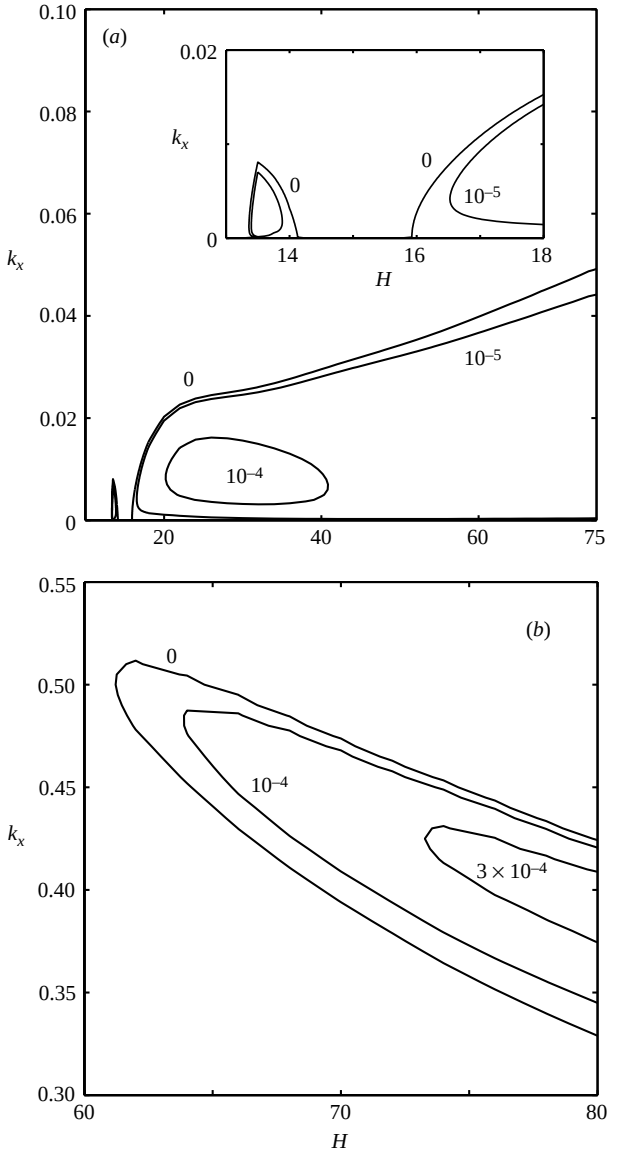

FIGURE 8. Contours of ω_r^l in the (H, k_x)-plane for the base state corresponding to the first pair of asymmetric solutions ($n = 1$) in figure 2(a). (a) Phase diagram, delineating the stable and unstable regions, for long waves. The inset shows this for small H in an expanded form. (b) Phase diagram at moderate values of k_x.

are shown in panel (a), and those for moderate k_x in the bottom one. The inset in figure 8(a) displays this for small H in an expanded form. It is observed from the inset that this instability arises beyond $H = H_c \approx 13.35$ due to long waves, but interestingly it disappears for a small range of Couette gaps for $14.2 < H < 16$. However, the flow again becomes unstable to long waves for $H > 16$. Note that the range of unstable k_x increases with increasing H. Figure 8(b) clearly shows that instabilities at moderate k_x are also possible when $H > 61$, and their growth rates are higher by an order of magnitude compared to those for long waves. In a stability map such as in

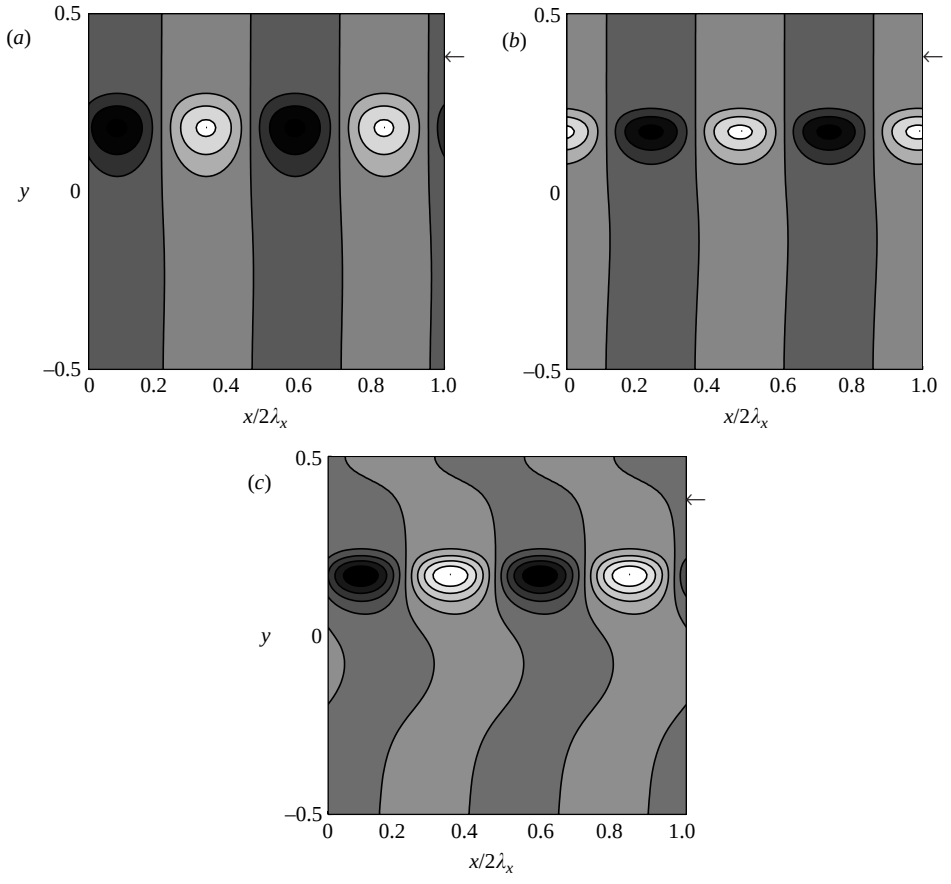

FIGURE 9. Density patterns for the unstable modes in figures 7(*a*) and 7(*b*). (*a*) Long-wave (dominant) forward travelling mode at $H = 50$ and $k_x = 0.0096$. (*b*) Long-wave forward travelling mode at $H = 75$ and $k_x = 0.01$. (*c*) Dominant forward travelling mode at $H = 75$ and $k_x = 0.42$. The arrow in each panel indicates the location where the base-state solid fraction is 0.649.

figure 8(*b*), the unstable region at moderate k_x is due to the second peak of the growth-rate curve in figure 7(*b*). It is, thus, clear that *even though the first pair of asymmetric solutions, having a plug near either of the walls, is stable to layering disturbances, it is unstable if the streamwise wavenumber, k_x, is small enough*, i.e. to *long-wave* travelling disturbances.

Let us now look at the eigenfunctions of the unstable modes. Figure 9(*a–c*) shows the disturbance patterns of solid fraction in the (x, y)-plane for the unstable modes of figures 7(*a*) and 7(*b*). On the grey scale, black represents maximum density and white minimum; the contours are drawn at equal intervals of solid fraction. The arrow in each panel shows the location where the base-state solid fraction is 0.649, i.e. the corresponding base state has a plug near the top wall. There is one row of particle clusters in each pattern, located above the mid-plane. (Note that we have used the term 'cluster' to denote a packet of density inhomogeneities over the base state.) Comparing the patterns in panels (*a*) and (*b*), we find that clusters shrink in size in the transverse direction as H is increased. The unstable pattern in panel (*c*), which is

due to the second peak in figure 7(*b*), consists of density bands which are a little more modulated than those in panel (*b*). Note that the x-coordinate has been normalized by twice the streamwise wavelength (λ_x) in all three panels of figure 9, and hence each pattern should be stretched by a factor $4\pi/k_x$ in the streamwise direction to ascertain the true inclination of the underlying density bands. All three patterns represent travelling wave modes, propagating in the streamwise direction with a phase velocity $c_{ph} \approx 0.5$. The base-state velocities at the centres of the clusters are lower than the respective phase velocities. Thus, the clusters move faster than the local mean flow. For the base state with a plug near the bottom wall, the unstable disturbance pattern is a backward propagating mode, due to the symmetry of the base states (4.1), which is simply a 180°-rotation of the corresponding forward propagating mode in figure 9.

4.2. *Effect of gravity on the stability of plugs*

Now we probe the stability of the gravitational Couette flow, focusing on base states at $(H, \overline{\nu}) = (25, 0.3)$ with adiabatic walls (i.e. no-slip and zero-heat-flux boundary conditions). (The results on the stability of dense flows such as those in figure 6 (i.e. at $\overline{\nu} = 0.5$) are similar to those at $\overline{\nu} = 0.3$, and hence we omit them.)

Figures 10(*a*) and 10(*b*) show the variation of the growth rate of the least stable mode, ω_r^l, with k_x at $Fr = 1000$ and 300, respectively. The solid/dot-dash line in each panel corresponds to the base state with a plug near the top/bottom wall as in figure 4. For a direct comparison, we have also displayed their variation for the gravity-free case, denoted by a dashed line in each panel. It is observed that all these plugged states are unstable to long-wave disturbances irrespective of the presence of gravity. The corresponding variation of the phase velocity (see the inset in panel *a*) suggests that these instabilities are 'travelling' waves with phase velocities close to 0.48. The inclusion of gravity in panel (*a*) acts to further stabilize/destabilize the base state with a plug near the bottom/top wall by reducing/enhancing the growth rate of its dominant mode. And decreasing the value of the Froude number to $Fr = 300$ enhances the above effect substantially as observed in panel (*b*). This panel also shows an interesting dichotomy in that there is a very narrow range of wavenumbers around $k_x \sim 0.021$ for which the solution with a bottom plug could be more unstable than the one with a top plug.

To find out whether the bottom-plug solution remains unstable with decreasing Fr, we have superimposed the growth-rate curves for two base flows at $Fr = 200$ and 100 in figure 10(*b*); other parameters are the same as for $Fr = 300$. (Recall that for these parameter combinations the unique base-flow solution having a bottom plug exists for $Fr < 240$.) We observe that the unique solution at $Fr = 200$ remains unstable to long waves, but becomes stable at $Fr = 100$. This observation holds for other values of $\overline{\nu}$ and e. Thus, the unique 'bottom-plug' solution can be unstable to long-wave 'travelling' disturbances, but will eventually become stable at sufficiently low values of Fr.

In figure 11(*a*, *b*), we display the perturbation density fields in (x, y)-plane for the dominant modes in figure 10(*b*) at $Fr = 300$; we have also superimposed the corresponding velocity patterns as vector plots in each panel. Note that the contour levels of density are the same in both panels. Each unstable mode represents a row of clusters with the perturbation density being maximum at $y \sim \pm 0.22$. However, there is a discernible difference between the unstable patterns for the base states with a plug near the top and bottom walls. For example, the density perturbation penetrates more into the top plug than the bottom one, and the cluster size for the former is much larger than for the latter, as also confirmed from a comparison between the

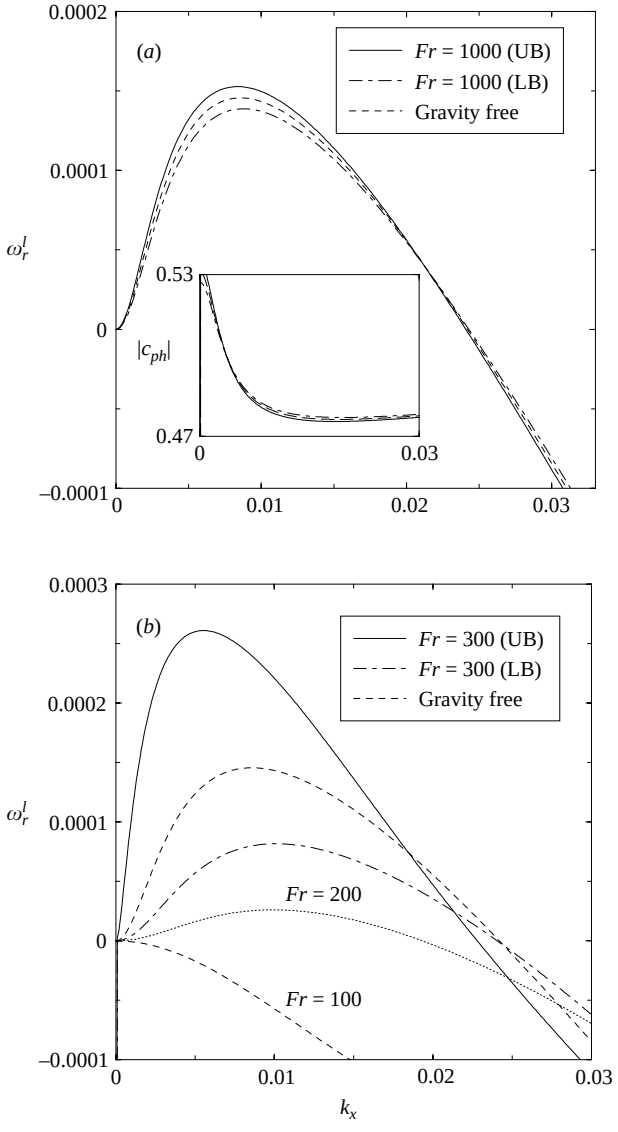

FIGURE 10. Effect of gravity on the variation of ω_r^l with k_x at (*a*) $Fr = 1000$ and (*b*) $Fr = 300$. Other parameters are $H = 25$, $\overline{v} = 0.3$ and $e = 0.8$. UB and LB refer to upper and lower parts of the $n = 1$ solution branches in figures 2(*c*) and 2(*g*), respectively. The inset in panel (*a*) shows the variations of phase velocity. In panel (*b*) the two bottom-most curves correspond to $Fr = 200$ and 100.

velocity fields in both panels. The perturbed motion consists of one pair of counter-rotating vortices per wavelength, with the velocity field inside each vortex being highly streamlined along the streamwise direction, except near the edge of the vortex.

Since our plugged solutions are unstable to long-wave ($k_x \sim 0$) 'travelling' disturbances, it is interesting to look for a possible connection with the recent work of Mitarai & Nakanishi (2004) on density-wave formation down an inclined chute (whose base state also has a plug near the rigid surface). They clearly showed that the instability of such plugged solutions is a consequence of the long-wave instability of

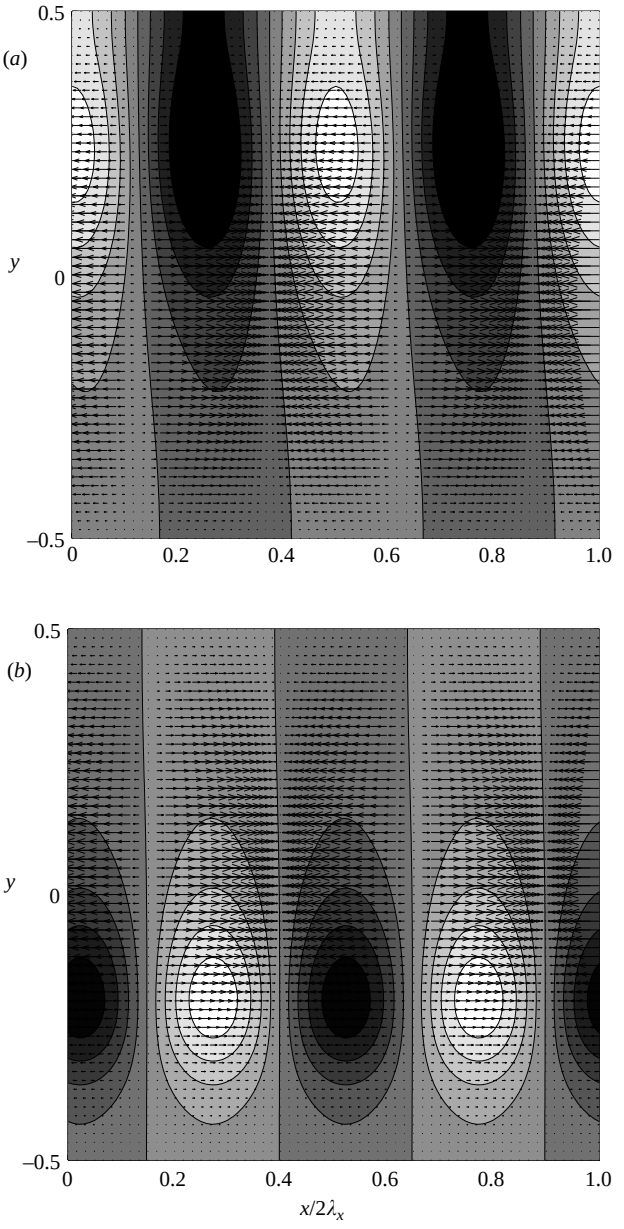

FIGURE 11. Comparison of density and velocity patterns for the dominant unstable modes in figure 10(*b*): $Fr = 300$. (*a*, *b*) Upper branch: $k_x = 0.0055$; (*c*, *d*) lower branch: $k_x = 0.0101$. On the grey scale, black represents maximum density and white minimum.

kinematic waves in an effective quasi-one-dimensional system. Following an identical mathematical procedure, a similar set of equations for the 'depth-averaged' density and streamwise velocity fields can be obtained for the plane Couette flow – refer to Mitarai & Nakanishi for related details. This similarity indicates that the observed long-wave instabilities of the plugged solutions in plane Couette flow are also of kinematic origin, and of the same class as those in chute flows.

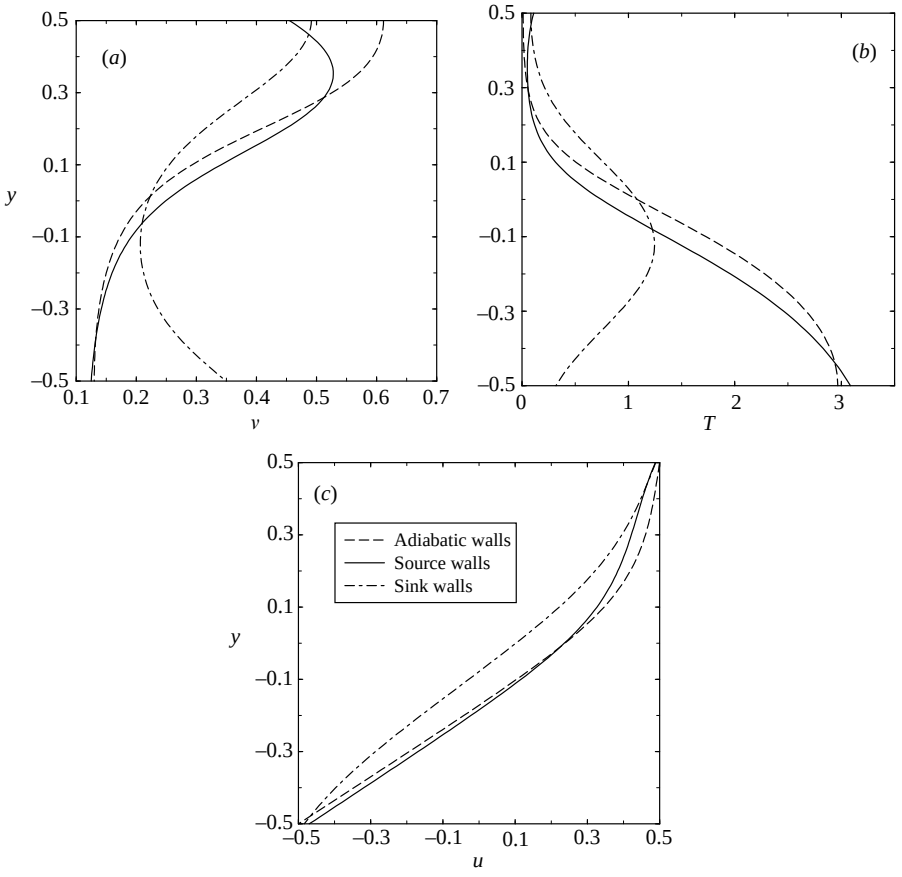

FIGURE 12. Effect of boundary conditions on the profiles of $v(y)$, $T(y)$ and $u(y)$ for the first pair of asymmetric solitions ($n=1$). The solid, dashed and dot-dashed lines correspond to source ($e_w=0.97$), adiabatic ($e_w=1.0$) and sink ($e_w=0.8$) walls, respectively. The parameter values are $\overline{\nu}=0.3$, $e=0.8$, $H=25$ and $Fr=1000$.

5. Discussion: boundary effects

Here we discuss the possible effects of boundary conditions on the bifurcating solutions and their stability to two-dimensional perturbations. For the sake of brevity, we will focus only on the $n=1$ bifurcation branch in figure 2(c) (i.e. $Fr=1000$), with a plug near the top wall. (The results for base states with a plug near the bottom wall are similar.) The material is now allowed to slip with inelastic particle–wall collisions. Recall that the wall slip leads to a production of granular energy and the inelastic particle–wall collisions dissipate that energy, and the relative dominance of one over the other will determine whether the walls act as a source or sink of granular energy.

Figure 12(a–c) shows the profiles of solid fraction, granular temperature and the streamwise velocity, with the parameter values $\overline{\nu}=0.3$, $e=0.8$, $H=25$ and $Fr=1000$. The value of the specularity coefficient ϕ has been set to 0.6 (as in Alam & Nott 1998) which corresponds to a rough wall for which the amount of slip is small ($u_s\sim 1/\phi$). (By decreasing the value of ϕ to 0.4, corresponding to a relatively smooth wall with larger wall slip, our results remain qualitatively similar.) The dashed line in each panel corresponds to the case of adiabatic walls for which no-slip and zero-heat-flux

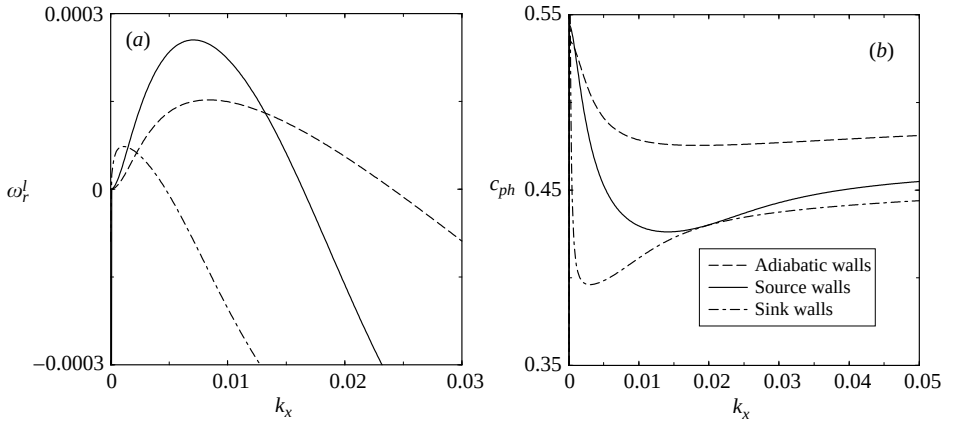

FIGURE 13. Effect of boundary conditions on the variations of (*a*) ω_r^l and (*b*) c_{ph} with k_x for the least-stable mode. The base states are shown in figure 12.

boundary conditions are imposed. For the case of nearly elastic wall–particle collisions $e_w = 0.97$, denoted by solid lines, the density profile is slightly modulated near the top wall in that the maximum density occurs in the bulk in contrast to at the top wall for the adiabatic wall case, and the corresponding temperature profile is modified accordingly; we also observe finite values of wall slip in panel (*c*). Since both walls are at a higher temperature than the bulk (along with positive temperature and density gradients at walls), there is a net flow of granular energy from the walls to the bulk. This implies that the walls act as a source of granular energy, and hence we call them source walls. For the case of moderately dissipative wall–particle collisions $e_w = 0.8$ (denoted by dot-dash lines), however, both density and temperature profiles look vastly different from their adiabatic counterparts, implying that the wall effects have influenced the bulk flow behaviour. It is clear from the corresponding temperature profile that there is a net flow of energy from the bulk to the walls, i.e. the walls now act as a sink of granular energy, and hence we call them sink walls.

Note that the influence of an energy source on the bottom plug is merely to push it into the bulk, with the plug being supported by a relatively dilute region near the wall. (The coexistence of a dense plug above a dilute 'sheared' region has been experimentally observed in inclined chute flows; see, for example, Johnson & Jackson 1987.) In fact, the non-adiabatic boundary conditions act as imperfections in an otherwise ideal system as detailed in Nott *et al.* (1999), but the overall bifurcation diagram and the related solution structures remain qualitatively similar to those for adiabatic walls.

Returning to the stability results of the above base states, we show the variations of ω_r^l and c_{ph} with k_x in figures 13(*a*) and 13(*b*), respectively. The dashed line corresponds to the base state with adiabatic walls ($e = 0.8$ and $e_w = 1$), while the solid and dot-dashed lines correspond to base states with source ($e_w = 0.97$) and sink ($e_w = 0.8$) walls, respectively. It is observed that the base states for all three cases remain unstable but for sink walls the growth rates are smaller by an order of magnitude. We have checked that by further reducing the particle–wall restitution coefficient to $e_w = 0.5$ the flow becomes stable to all wavenumbers. This is presumably due to the fact that the smaller the value of e_w (with other parameters being fixed), the larger the amount of energy that the sink walls would extract from the mean flow, thereby making the flow more stable. This observation is in tune with earlier stability results

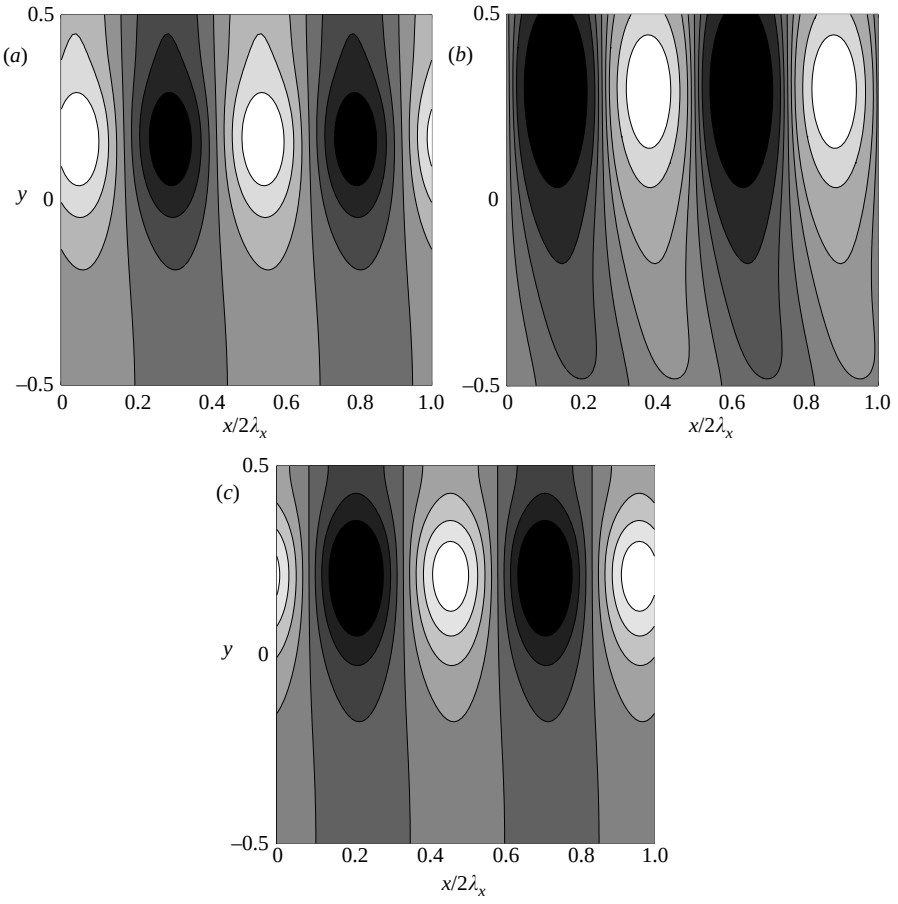

FIGURE 14. Comparison of density patterns for the dominant unstable modes in figure 13. (*a*) Source walls: $k_x = 0.0071$; (*b*) sink walls: $k_x = 0.0011$; (*c*) adiabatic walls: $k_x = 0.0084$. On the grey scale, black represents maximum density and white minimum.

of Alam & Nott (1998) with plugged base states. We further note in figure 13(*a*) that even though the growth rate of the dominant mode for source walls is larger than that for adiabatic walls, the range of corresponding unstable k_x is relatively smaller. From the phase-velocity curves, we find that the dominant instability in each case represents a forward travelling wave, and this instability travels at a relatively lower phase velocity for non-adiabatic walls compared to its adiabatic counterpart.

Density patterns corresponding to the dominant unstable modes in figure 13 are shown in figure 14(*a–c*) for source, sink and adiabatic wall conditions. Note that the contour levels are the same for all three cases. We observe that the clustering pattern for the source-wall case looks similar to that of the adiabatic case, but it differs significantly for sink walls in that the region of influence of the perturbation density is much larger. This apparent dissimilarity in the structure of particle clusters can be attributed to the differences in their respective base-state profiles. For example, the variation of the base-state density across the Couette gap for the case of sink walls is relatively more uniform than its adiabatic- and source-wall counterparts (cf. figure 12*a*). This in turn helps the perturbation fields to penetrate further in the transverse direction, thereby increasing the cluster size.

It is clear from the above discussion that the qualitative nature of our results would not change even if we impose wall-slip and non-zero heat-flux boundary conditions, and for details on related issues (without gravity) the reader is referred to Nott *et al.* (1999).

6. Summary and conclusions

We have investigated the instability-induced ordering phenomenon and the influence of gravity on it in the plane Couette flow of granular materials using a kinetic-theory rheological model. For the gravity-free case, the uniform shear state (having uniform density, temperature and shear rate throughout) is a solution of the equations of motion which is known to be unstable to purely streamwise disturbances ($k_x = 0$). These stationary instabilities give birth to new steady solutions, having ordered density patterns of alternating bands of dense and dilute regions along the transverse direction, through an infinite hierarchy of pitchfork bifurcations.

The effect of gravity can be included in the plane Couette flow with the Froude number ($Fr = \tilde{u}_w/(\tilde{g}\tilde{d})^{1/2} = \tilde{\gamma}\tilde{\tau}_d$, where $\tilde{\gamma} = \tilde{u}_w/\tilde{H}$ is the imposed shear rate and $\tilde{\tau}_d = H(\tilde{d}/\tilde{g})^{1/2}$ is the gravitational time scale) being the continuation parameter. With other parameters fixed, the increasing gravitational effects can be equated with decreasing either the value of the Froude number Fr or the imposed shear rate. For the steady fully developed plane Couette flow, the inclusion of gravity destroys the centre-symmetry (i.e. $\nu(y) = \nu(-y)$, $T(y) = T(-y)$ and $u(y) = -u(-y)$) of its gravity-free counterpart, and the equations of motion now allow only asymmetric solutions. Thus, gravity acts as an imperfection in the problem, destroying the 'perfect' bifurcation structure of the uniform shear flow. The degree of imperfection increases with decreasing shear rate and vice versa. We have shown that the present bifurcation problem admits the 'universal' unfolding of pitchfork bifurcations, implying that all possible scenarios of imperfect bifurcations are hidden in our gravitational Couette flow (as discussed in the Appendix). The unfolding of bifurcations subsequently leads to the formation of a sequence of a countably infinite number of isolas. The solution structures associated with these isolas are modulated versions of their gravity-free counterparts. With decreasing values of Fr, these isolas shrink in size and disappear subsequently from the phase space, implying that the gravity does not support the related solutions. For sufficiently small values of Fr (i.e. low shear rates), we have found that the only solution branch which survives in the phase space corresponds to solutions having a plug near the bottom wall, in which the particles are densely packed and the shear rate is close to zero, and a uniformly sheared dilute zone above it. This is precisely what one always observes in shear-cell experiments. Interestingly, a stable plug can also be maintained near the top wall if the shear rate is large. In this case, the gradient of the dispersive normal pressure, due to the shear-induced fluctuations, is strong enough to overcome the barrier of weak gravitation, making the plugs floating (and stable) away from the bottom wall. Thus, we have established that the plug formation in gravitational Couette flows is tied to the instability-induced ordering phenomenon in the closely related uniform shear flow. This conclusion remains unaltered even if we include wall-slip and non-zero-heat-flux boundary conditions.

We have explicitly shown that the effect of gravity on the non-uniform solutions in the rapid flow regime do give rise to the shear-banding-type solutions that are typically encountered in the Earth-bound shear-cell experiments (i.e. in the slow dense regime). Hence, both appear to have the same origin.

It is remarkable that a rheological model based on kinetic theory arguments predicts a flow regime of dense plugs where the validity of some of its built-in assumptions

(binary collisions, molecular chaos, etc.) cease to hold. For such dense plugs where the particles are closely packed, multi-particle collisions and Coulomb friction are likely to be important and should be incorporated in the rheological model (Luding & Goldshtein 2003; Alam & Luding 2003). In this regard, we recall the work of Alam & Nott (1997), based on a phenomenological frictional–kinetic model, who found that the layering instabilities also survive even if we include Coulomb friction, and hence we expect a similar bifurcation scenario leading to plug formation as in the present case. Hence the associated hydrodynamic equations of rapid flows do form the 'minimal' set, and the additional effects of dense rheology can be incorporated through the constitutive model. Despite ignoring friction, however, our predictions of mean fields are quite sensible from the viewpoint of published results on shear-cell experiments (at low shear rates). At larger shear rates, we have also found 'floating' plugs which remains to be verified under experimental conditions. Extensive molecular dynamics simulations should be carried out to make a direct quantitative comparison between simulation and theory. Another possibility is to conduct the Couette-shear experiments under microgravity conditions to realize such plugged states.

A two-dimensional linear stability analysis of the plugged base states showed that they are stable to purely streamwise disturbances but may become unstable to long-wave ($k_x \sim 0$) travelling disturbances. The effect of gravity is simply to further stabilize or destabilize the plugged base state (compared to its gravity-free counterpart) depending whether the plug is located near the bottom or top wall, respectively. The unique base-flow solution having a bottom plug remains stable at sufficiently low shear rates. Interestingly, a 'floating' plug near the top wall (at high shear rates) can also be stable if the wavelength of the disturbance is of moderate value (i.e. $k_x \sim O(1)$ and larger). Preliminary work on the purely streamwise three-dimensional instability ($k_x = 0$, with non-zero spanwise wavenumber k_z) of bounded uniform shear flow (Alam 2004*b*) suggests that this flow supports streamwise vortices with the dominant unstable spanwise wavenumber being of order $k_z \sim O(1)$. Such coherent vortices will clearly lead to particle reorganization in the Couette cell; however, their effects on plugged base states remain unexplored. It would be desirable to further investigate the stability of these base states to three-dimensional perturbations, complemented by molecular dynamics simulations. Work in these directions is in progress.

Since the shear-banding phenomenon in gravitational Couette flow that we have uncovered is tied to the instability-induced ordering in its gravity-free counterpart, it is interesting to ask whether the predicted instabilities are of constitutive origin. There is a vast body of literature, mainly in polymer rheology and solid mechanics, where the nonlinearities in constitutive laws lead to instabilities, commonly known as constitutive instability (Hadamard 1903). These instabilities are quite different from their well-known hydrodynamic, counterpart for which the nonlinearities associated with inertial terms are responsible for the onset of instability. That the layering instabilities of uniform shear flow are indeed of constitutive origin has been established (Goddard & Alam 1999). More specifically, the non-monotonicity of the shear-to-normal stress ratio with density gives rise to these instabilities. The present work thus goes a step further by looking at the effects of gravity and boundary conditions on constitutive instabilities and their nonlinear saturation.

M. A. would like to thank A. S. Vasudeva Murthy (Tata Institute for Fundamental Research, Bangalore) for hospitality, where the work on gravitational effects was initiated. Later on, this work was continued sporadically at various places (UC San Diego (NASA/NAG 3-1888, for a travel-grant to attend the 51st Annual

APS Meeting of the DFD at Philadelphia, 1998); ICA1, Universität Stuttgart (Alexander von Humboldt Fellowship)), and eventually completed at the JNCASR. M.A. acknowledges related partial financial supports from the JNCASR and the above agencies.

Appendix. Imperfections and the universal unfoldings of pitchfork bifurcation and isola-centre

A bifurcation problem with one state variable (order parameter) θ and a bifurcation (control) parameter R can be formulated as

$$\frac{\mathrm{d}\theta}{\mathrm{d}t} = f(\theta, R), \tag{A 1}$$

where $f(\theta, R)$ is a scalar-valued function. The set of (θ, R) satisfying $f(\theta, R) = 0$ is called the bifurcation diagram. For pitchfork bifurcations, the scalar-valued function is a cubic in θ:

$$f(\theta, R) = \theta^3 - R\theta = -f(-\theta, R),$$

which satisfies the basic property that as the bifurcation parameter R crosses some critical value R_c, the number of solutions jumps from one to three.

Imperfections hidden in an otherwise ideal system lead to imperfect bifurcations, whose study deals with the changes of (A 1) subject to perturbations, resulting in changes in the associated bifurcation diagrams. In the realm of singularity theory, the general problem of imperfect bifurcation is addressed by using the theory of universal unfolding. The normal-form equation for the universal unfolding of pitchfork bifurcation is given by (Golubitsky & Schaeffer 1985):

$$\frac{\mathrm{d}\theta}{\mathrm{d}t} = \theta^3 - R\theta + \alpha + \beta\theta^2 = F(\theta, R; \alpha, \beta), \tag{A 2}$$

where the order parameter θ, for the present problem, can be tied to $\theta = v_{tw}$, or $(v_{tw} - \overline{v})$ or any other suitable quantity, and the bifurcation parameter to $R \equiv R(H, e, \overline{v})$. Here α and β are called imperfections, and both of them vanish identically for 'perfect' pitchfork bifurcations. Without delving into deriving the exact normal-form equation for the granular Couette flow, here we simply consider the possible functional forms of the associated coefficients in (A 2) to facilitate our discussion on universal unfolding. From the base-flow equations (2.7), we see that α and β are functions of Fr, H and ν, i.e.

$$\alpha \equiv \alpha(Fr^{-1}, H, \nu) \quad \text{and} \quad \beta \equiv \beta(Fr^{-1}, H, \nu),$$

with the following property:

$$\alpha(0, H, \nu) = 0 = \beta(0, H, \nu),$$

that corresponds to the ideal case of 'perfect' pitchfork bifurcations for which

$$F(\theta, R; 0, 0) \equiv f(\theta, R).$$

The function $F(\theta, R; \alpha, \beta)$ can be thought of as a perturbation of the scalar-valued function $f(\theta, R)$, and is called the universal unfolding of $f(\theta, R)$ since it encompasses all possible forms of imperfect pitchfork bifurcations.

The universal unfolding of the pitchfork leads to four possible bifurcation diagrams in the (α, β)-plane (Golubitsky & Schaeffer 1985). In fact, two curves $\alpha = 0$ and $\alpha = \beta^3/27$, denoted by thick solid lines in figure 15, divide the (α, β)-plane into four

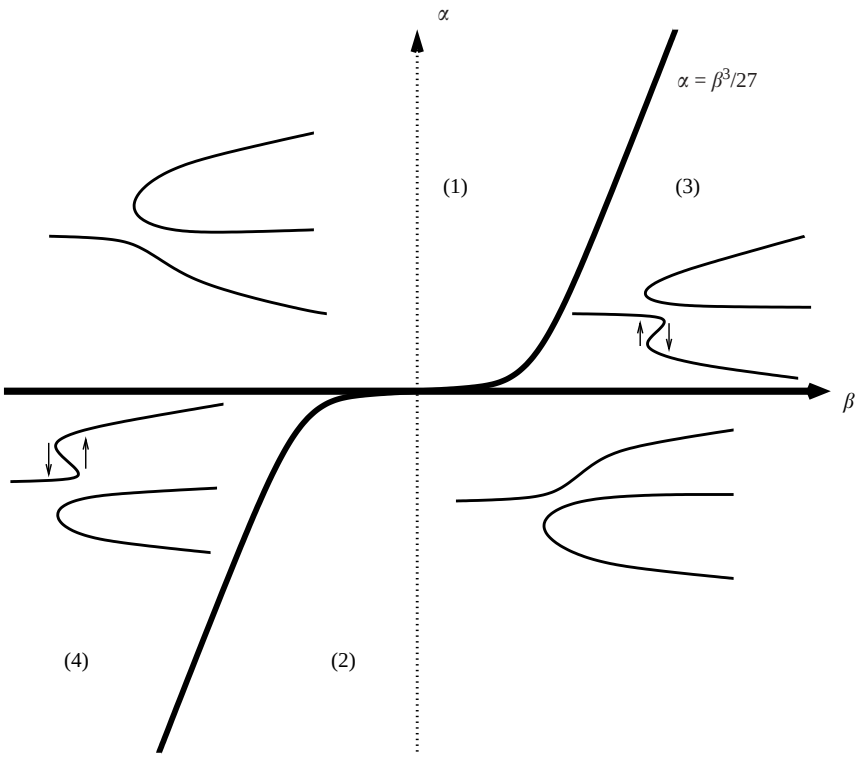

FIGURE 15. Schematic of the universal unfolding of pitchfork bifurcations. All four cases of imperfect bifurcations are present in granular Couette flow.

zones, and all parameter combinations in each zone represent a canonical bifurcation diagram as shown schematically in this figure. Comparing our bifurcation diagrams in figures 2 and 5 with these four sets, we find that the bifurcation diagram for zone 1 represents the unfolding of pitchfork bifurcations in our cases. However, if we redefine our order-parameter as $\theta = \nu_{bw} \equiv \nu(-1/2)$, i.e. the value of the solid fraction at the bottom wall, and redraw the bifurcation diagrams of figures 2 and 5, we get back the canonical set for zone 2 since the smooth solution branch now arises from the upper part of the corresponding $n = 1$ bifurcation branch of the gravity-free case. This is due to the invariance of the normal-form (A 2) to the transformation $(\theta, \alpha, \beta) \rightarrow -(\theta, \alpha, \beta)$.

Recall that the layering instabilities in granular Couette flow also lead to subcritical pitchfork bifurcations (Nott *et al.* 1999) that occur at lower mean densities (see their figures 6*e* and 6*f*). The inclusion of gravity on these subcritical bifurcations would naturally recover the remaining two 'hysteretic' bifurcation diagrams (Alam 2004*a*) for zone 3 and zone 4 in figure 15. Thus, we conclude that the gravitational Couette flow admits all four cases of the universal unfolding of pitchfork bifurcations.

Lastly, we consider an isola-centre and its unfolding 'isola'. An isola-centre is defined as a singularity of codimension one, and its universal unfolding results in an isola for which the normal-form equation is given by

$$\frac{\mathrm{d}\theta}{\mathrm{d}t} = \theta^2 + R^2 + \alpha = F(\theta, R; \alpha). \tag{A 3}$$

Note that $\alpha = 0$ represents an isola-centre and $\alpha < 0$ an isola; clearly, there is no solution to (A 3) for $\alpha > 0$. Of course, for the present problem, isolas appear as a consequence of imperfect pitchfork bifurcations under strong perturbations (i.e. for large values of Fr^{-1}).

REFERENCES

Alam, M. 1998*a* Stability of unbounded and bounded granular shear flows. PhD thesis, Indian Institute of Science, Bangalore, India.

Alam, M. 1998*b* The role of gravity on granular shear flow: steady flow, bifurcation and stability. *Bull. Am. Phys. Soc.* **43**, 2009.

Alam, M. 2003 Pattern formation in rapid-shear granular Couette flow. In *Advances in Fluid Mechanics* (ed. M. Alam, R. Govindarajan, R. Ramesh & K. R. Sreenivas), pp. 150–160, JNCASR, Bangalore, India.

Alam, M. 2004*a* Universal unfolding of pitchfork bifurcations and the shear-banding instabilities in rapid granular Couette flow. In *Symposium on Trends in Applications of Mathematics to Mechanics'04, 22–28 August, Seeheim, Darmstadt, Germany* (ed. K. Hutter & Y. Wang). Shaker-Verlag.

Alam, M. 2004*b* Streamwise vortices and density patterns in rapid granular Couette flow: a linear stability analysis. *Preprint*.

Alam, M. & Luding, S. 2003 First normal stress difference and crystallization in a dense sheared granular fluid. *Phys. Fluids* **15**, 2298.

Alam, M. & Nott, P. R. 1997 The influence of friction on the stability of unbounded granular Couette flow. *J. Fluid Mech.* **343**, 267.

Alam, M. & Nott, P. R. 1998 Stability of plane Couette flow of a granular material *J. Fluid Mech.* **377**, 99.

Babić, M. 1993 On the stability of rapid granular flows. *J. Fluid Mech.* **254**, 127.

Campbell, C. S. 1990 Rapid granular flows. *Annu. Rev. Fluid Mech.* **22**, 57.

Drazin, P. G. & Reid, W. H. 1985 *Hydrodynamic Stability*, Cambridge University Press.

Forterre, F. & Pouliquen, O. 2002 Stability analysis of rapid granular chute flows: formation of longitudinal vortices. *J. Fluid Mech.* **467**, 361.

Goddard, J. & Alam, M. 1999 Shear-flow and material instabilities in particulate suspensions and dry granular media. *Particulate Sci. Tech.* **17**, 69.

Goldfarb, D., Glasser, B. & Shinbrot, T. 2002 Shear instabilities in granular flows. *Nature* **415**, 302.

Golubitsky, M. & Schaeffer, D. 1985 *Singularities and Groups in Bifurcation Theory* I. Springer.

Hadamard, J. 1903 *Lecons sur la Propagation des Ondes et les Équations de l'Hydrodynamique*. Paris. (Chelsea Publishing Company: New York, Reprinted in 1949)

Hayakawa, H. 2003 Hydrodynamics of driven granular gases. *Phys. Rev. E* **68**, 031304.

Herrmann, H. J., Hovi, J.-P. & Luding, S. 1998 *Physics of Dry Granular Media*. Kluwer.

Hopkins, M. A. & Louge, M. Y. 1991 Inelastic microstructure in rapid granular flows of smooth disks. *Phys. Fluids* A **3**, 47.

Hutter, K. & Rajagopal, K. R. 1994 On flows of granular materials. *Continuum Mech. Thermodyn.* **6**, 81.

Jaeger, H. M., Nagel, S. R. & Behringer, B. 1996 Granular solids, liquids and gases. *Rev. Mod. Phys.* **68**, 1259.

Jenkins, J. T. & Richman, M. W. 1986 Boundary conditions for plane flows of smooth, nearly elastic, circular disks. *J. Fluid Mech.* **171**, 53.

Johnson, P. C. & Jackson, R. 1987 Frictional-collisional constitutive relations for granular materials, with application to plane shearing. *J. Fluid Mech.* **176**, 67.

Kadanoff, L. 1999 Built upon sand: Theoretical ideas inspired by granular flows. *Rev. Mod. Phys.* **64**, 111.

Luding, S. & Herrmann, H. J. 1999 Clustering in granular gases. *Chaos* **9**, 673.

Luding, S. & Goldshtein, A. 2003 Collisional cooling with multiparticle interactions. *Granular Matter* **5**, 159.

Lun, C. K. K., Savage, S. B, Jeffrey, D. J. & Chepurniy, N. 1984 Kinetic theories for granular flow: inelastic particles in Couette flow and slightly inelastic particles in a general flow field. *J. Fluid Mech.* **140**, 223.

Mitarai, N. & Nakanishi, H. 2004 Linear stability analysis of rapid granular flow down a slope and density wave formation. *J. Fluid Mech.* **507**, 309.

Nott, P. R., Alam, M., Agrawal, K., Jackson, R. & Sundaresan, S. 1999 The effect of boundaries on the plane Couette flow of granular materials: a bifurcation analysis. *J. Fluid Mech.* **397**, 234.

Olmsted, P. D. & Lu, C. Y. D. 1997 Coexistence and phase separation in sheared complex fluids. *Phys. Rev.* E **56**, R55.

Peng, G. & Herrmann, H. J. 1996 Density waves and $1/f$ density fluctuations in granular flow. *Phys. Rev.* E **51**, 1745.

Pöschel, T. & Luding, S. 2001 *Granular Gases*. Lecture Notes in Physics, vol. 564. Springer.

Sasvari, M., Kertesz, Y. & Wolf, D. 2000 Instability of symmetric Couette flow in a granular gas: Hydrodynamic field profiles and transport. *Phys. Rev.* E **62**, 3817.

Savage, S. B. 1992 Instability of unbounded uniform granular shear flow. *J. Fluid Mech.* **241**, 109.

Savage, S. B. & Sayed, M. 1984 Stresses developed by dry cohesionless granular materials sheared in an annular shear cell. *J. Fluid Mech.* **142**, 391.

Schmid, P. J. & Kytömaa, H. K. 1994 Transient and asymptotic stability of granular shear flow. *J. Fluid Mech.* **264**, 255.

Sela, N. & Goldhirsch, I. 1998 Hydrodynamic equations for rapid shear flows of smooth, inelastic spheres, to Burnett order. *J. Fluid Mech.* **361**, 41.

Tan, M.-L. 1995 Microstructures and macrostructures in rapid granular flows. PhD thesis, Princeton University, USA.

Thompson, P. A. & Grest, G. S. 1991 Granular flow: friction and the dilatancy transition. *Phys. Rev. Lett.* **67**, 1751.

Wang, C., Jackson, R. & Sundaresan, S. 1996 Stability of bounded rapid shear flows of a granular material. *J. Fluid Mech.* **308**, 31.

Zhang, C. & Campbell, C. S. 1992 The interface between fluid-like and solid-like behaviour in two-dimensional granular flows. *J. Fluid Mech.* **237**, 541.